



**HAL**  
open science

# Simulation of Isolated and Installed Jet Noise at Mach = 0.9: Influence of Numerical Mesh and Physical Insights

Maxime Huet, Fabien Gand, Gilles Rahier

## ► To cite this version:

Maxime Huet, Fabien Gand, Gilles Rahier. Simulation of Isolated and Installed Jet Noise at Mach = 0.9: Influence of Numerical Mesh and Physical Insights. Flow, Turbulence and Combustion, 2023, "Special Issue": Installation effects on jet aeroacoustics, 10.1007/s10494-023-00461-y . hal-04192131

**HAL Id: hal-04192131**

**<https://hal.science/hal-04192131>**

Submitted on 31 Aug 2023

**HAL** is a multi-disciplinary open access archive for the deposit and dissemination of scientific research documents, whether they are published or not. The documents may come from teaching and research institutions in France or abroad, or from public or private research centers.

L'archive ouverte pluridisciplinaire **HAL**, est destinée au dépôt et à la diffusion de documents scientifiques de niveau recherche, publiés ou non, émanant des établissements d'enseignement et de recherche français ou étrangers, des laboratoires publics ou privés.



Distributed under a Creative Commons Attribution 4.0 International License



# Simulation of Isolated and Installed Jet Noise at Mach = 0.9: Influence of Numerical Mesh and Physical Insights

Maxime Huet<sup>1</sup> · Fabien Gand<sup>2</sup> · Gilles Rahier<sup>1</sup>

Received: 3 November 2022 / Accepted: 17 July 2023  
© The Author(s) 2023

## Abstract

The noise radiated by an isothermal, single-stream jet with a Mach number  $M=0.9$  and diameter-based Reynolds number  $Re_D=10^6$  is investigated numerically without and with the presence of a flat plate. Noise sources are predicted with Zonal Detached Eddy Simulations yielding Wall Modelled LES in attached boundary layers (so called ZDES mode 3) together with turbulence tripping inside the nozzle to recover an initially turbulent flow, while radiated pressure is extrapolated with integral methods. Numerical methodology, namely grid and statistical convergence of the signals, is assessed for the isolated jet. Noise levels are accurately simulated at least up to  $St=8$  and integrated pressure levels collapse within 1 dB with the experiments. In the presence of the plate, a noise radiation methodology based on both Ffowcs Williams Hawkins and Kirchhoff integral methods is proposed to reconstruct the pressure signals at microphone locations with a reduced numerical cost. The simulation compares very favorably with the experimental data, azimuthal noise variations induced by the plate are correctly captured and noise levels collapse within 1 dB. It is concluded the numerical methodology is mature enough for application in an industrial context.

**Keywords** Jet noise · Installation noise · Computational fluid dynamics · Zonal detached eddy simulation · Integral methods

## 1 Introduction

Among all the noise sources of an aircraft, jet noise remains a dominant one and still requires a lot of attention. For an isolated jet the acoustic power follows the well-known Lighthill's power law, which predicts a variation of the power with the eighth power of the flow velocity (Lighthill 1954). Jet noise is therefore particularly strong during take-off, where a high power setting of the engine is required and results in a transonic, highly turbulent jet flow. The interested reader may refer to the reviews of Bailly and Kaji (2016) and Tam (2019) for details on isolated jet noise sources. During the last decades, important

---

✉ Maxime Huet  
maxime.huet@onera.fr

<sup>1</sup> DAAA, ONERA, Université Paris Saclay, 92322 Châtillon, France

<sup>2</sup> DAAA, ONERA, Université Paris Saclay, 92190 Meudon, France

jet noise reduction has been achieved by decreasing the jet velocity, first through the use of double stream nozzles, then by the increase of the bypass ratio of the engine, and therefore an increase of its size. When the engine is positioned close to the wing, the turbulent flow generates additional low-frequency noise known as jet installation noise or jet-surface interaction (JSI) noise (Head and Fisher 1976). For recent engines, the bypass ratio rises above 15 and leads to integration problem (Meloni et al. 2020; Tyacke et al. 2019) which increases the contribution of JSI noise.

Jet installation noise has been widely investigated experimentally over the years for both simplified (Head and Fisher 1976; Cavalieri et al. 2014; Lawrence and Self 2011; Piantanida et al. 2016; Bychkov and Faranosov 2018) and more realistic, industrial-like configurations (Perrino 2014; Lyubimov et al. 2014; Belyaev et al. 2017). Among others, Lawrence et al. performed an extensive experimental campaign for various axial and radial distances between the jet and the trailing edge of the plate as well as jet Mach number (Lawrence and M. A. and R. H. Self 2011). Results particularly evidence the sensitivity of noise production to the trailing edge position and the predominance of JSI noise for low velocity jets. Finally, by comparing jet installation noise issued from a flat plate or realistic wings, Lawrence experimentally found that jet data scale well between both configurations so that the jet-plate configuration is well suited for analytical, numerical and experimental investigations (Lawrence 2011).

From a theoretical point of view, Ffowcs Williams and Hall proved low-frequency noise is increased when flow turbulence is scattered by the trailing edge of the solid surface and radiates predominantly in the upstream direction (Ffowcs Williams and Hall 1970). This scattered noise scales with the fifth power of the flow velocity, which makes it dominant compared to the free-jet noise for low Mach numbers. Cavalieri et al. observed the scattered sound decreases exponentially with the increasing jet-plate distance and suggested it is produced by the scattering of evanescent hydrodynamic wavepackets in the jet (Cavalieri et al. 2014). The identification of turbulence scattering as the main mechanism of jet installation noise paved the way to analytical modelling of JSI noise (Cavalieri et al. 2014; Bychkov and Faranosov 2018; Vera et al. 2015; Lyu et al. 2017; Nogueira et al. 2017; Faranosov et al. 2019; Lyu and Dowling 2019). It is worth noting that, except when the plate is very close to the jet, the wavepacket structure is barely impacted by the presence of the solid surface and isolated jet data may be used to model installation noise, which results in a drastic reduction of the numerical/experimental effort to characterize the source (Cavalieri et al. 2014).

There are numerous examples of isolated jet aeroacoustics simulation in the literature (Freund 2001; Shur et al. 2005; Shur et al. 2005; Bodony and Lele 2005; Andersson et al. 2005; Uzun and Hussaini 2011; Bogey et al. 2011). Despite the rapid increase of computational power, the cost of Direct Numerical Simulation (DNS) still remains prohibitive for large scale or complex configurations. For large Reynolds number jet flows, Large Eddy Simulation (LES) represents a good option because it allows the resolution of large scale turbulent structures, responsible of turbulent energy production, and therefore noise generation, whereas small-scale turbulence is assumed to be isotropic and is modelled. A key element for the numerical resolution of jet flow is the numerical grid. Generally speaking, there are two main approaches available using either block-structured grids or unstructured grids. Numerical schemes usually present a better accuracy for structured grids but the discretization of complex, industrial-like geometries is a complex task and the need of refinement in localized regions usually penalizes the total grid count because this refinement propagates along the whole mesh. Unstructured grids, on the contrary, make possible the clustering of the grid points in specific areas – which also compensates to some extent

the generally more dissipative properties of unstructured numerical schemes compared to structured ones—as well as an easier discretization of complex shapes and proved to be efficient for jet noise prediction (Zhu et al. 2018; Fosso Pouangué et al. 2015). The capacity of flow resolution inside the jet plume is nevertheless not sufficient by itself to accurately predict jet noise, as flow development is also driven by the state of the shear layer at nozzle exit, either laminar for low Reynolds number or turbulent for larger values. This phenomenon has been evidenced experimentally by Zaman (Zaman 1985; Zaman 1985) and numerically by Bogey et al. (Bogey et al. 2008, 2012) for instance. Initially laminar jets exhibit an additional noise source in the medium frequency range due to vortex pairings in the shear layer, that remain present for high Reynolds number jet if no turbulence is seeded in the boundary layer. Several solutions are available to trigger this boundary layer turbulence, such as the injection of small random velocity disturbances (Bogey et al. 2008, 2012, 2029), a turbulence rescaling-recycling procedure (Uzun and Hussaini 2009) or various synthetic turbulence methods (Bühler et al. 2014; Housman et al. 2017; Stich et al. 2021; Brès et al. 2018). In order to reduce the acoustic perturbations which can be generated by synthetic methods and mimic the experimental turbulence triggering devices, geometrical forcing can be considered (Zhu et al. 2018; Lorteau et al. 2014, 2015; Velden et al. 2019). The interested reader may refer to the review of Shur et al. for an overview of the existing approaches to create turbulent content in aeroacoustic simulations (Shur et al. 2014). Of interest, Deck et al. (Deck et al. 2018) have proposed a method based on roughness elements—or tripping dots— included in the computational domain with the Immersed Boundary Condition (IBC) (Mochel et al. 2014) to trigger turbulent transition mechanisms resolved with a Wall Modelled LES (WMLES) approach, namely the mode 3 of Zonal Detached Eddy Simulation (ZDES) (Deck 2012; Deck et al. 2014). This approach was successfully applied to jet flows in (Gand and Huet 2021) and the method appeared well suited for aeroacoustics applications.

Acoustic waves can be propagated to microphones locations in the CFD simulation, but this approach is unnecessarily expensive. Viscous and turbulent flow effects being negligible during propagation, which occurs essentially in uniform mean flows, a two-step procedure is classically employed where noise radiation is achieved as a post-processing with Computational AeroAcoustics (CAA) simulation (Bailly et al. 2010; Labbé et al. 2013) or with the help of integral methods (Lyrintzis 1994; Rahier et al. 2004). The Ffowcs Williams and Hawkings (FWH) integral method (Ffowcs Williams and Hawkings 1969) is particularly well suited for turbulent flows and is commonly used for isolated jets (Brès et al. 2018; Rahier et al. 2004; Gand et al. 2017; Lorteau et al. 2018; Rego et al. 2020). With this approach the far-field pressure fluctuations are reconstructed from the unsteady flow fields on a porous surface encompassing the noise sources for a very affordable numerical cost. This methodology remains valid in the presence of a wing and has been used by several authors (Tyacke et al. 2019; Bondarenko et al. 2012; Angelino et al. 2018, 2019; Stich et al. 2019; Wang et al. 2020; Silva et al. 2015; Rego et al. 2020). The numerical cost of the CFD simulation however becomes important when the wing span is large because all acoustic effects, including the propagation of acoustic waves up to the wing extremities, need to be accurately captured during the flow simulation. To address this issue, some authors couple the CFD simulation, dedicated to the production of noise and its propagation in the close vicinity of the jet and wing, with a CAA simulation that propagates noise around the wing towards a uniform mean flow where an integral method is used for the radiation to the far-field microphones (Gand et al. 2017; Davy et al. 2019). CAA simulations being cheaper than CFD ones for the propagation of acoustic waves with the same order of accuracy, this approach is expected to reduce the total computational cost. It nevertheless requires the

construction of a dedicated numerical grid for the CAA simulation and some engineering and numerical efforts to run the simulations. In the present study, an alternative procedure is applied for the first time on installed jet configurations using integral methods. Similarly to the isolated configuration, a porous surface is located in the vicinity of the jet plume to limit the computational cost of the CFD. Jet-plate interactions occurring inside the surface are captured by CFD and are taken into account in the noise radiated to the far-field through their contribution in the perturbation field on the porous surface whereas acoustic reflections on the flat plate outside the porous surface are modelled in the radiation process: the flat plate is represented as a solid surface in the noise simulation and the contribution of the reflections to the total radiated noise is computed with an integral method.

The article is organized as follows. The numerical methodologies for the generation of initially turbulent jet flows and their noise radiation with integral methods are detailed in Sect. 2. The isolated and installed jet test cases, corresponding to an isothermal, Mach 0.9 turbulent jet, are described in Sect. 3 together with the numerical settings for the simulations. Aerodynamic and acoustic assessment of the isolated simulation are provided in Sect. 4, together with a comparison of the present unstructured grid results with previously-performed structured grid simulations and an evaluation of the convergence of the statistical data. The installed jet is simulated in Sect. 5. The radiation method for jet-wing configuration is presented and validated against CFD results before flow and noise changes caused by the presence of the plate are discussed. To end, conclusions are drawn in Sect. 6.

## 2 Computational Methodologies

The hybrid RANS/LES method used in this work is the Zonal Detached Eddy Simulation (ZDES) (Deck 2012) developed at ONERA. This approach has been used with success to simulate a wide range of applications of industrial interest (Deck et al. 2014). One of the advantages of the ZDES is that it covers several types of detached flows, which can be combined. It is important to bear in mind that modes 1 and 2 of ZDES belong to the so-called “natural Detached Eddy Simulation” approaches in which the attached boundary layers are treated in RANS while free shear flows are resolved in LES. Conversely, mode 3 of ZDES is a Wall Modelled LES approach in which the outer part of attached boundary layers is resolved in LES. An example of the combined use of the three modes of ZDES within the same computation can be found in (Deck and Laraufie 2013). The complete formulation of ZDES mode 3, which is the operating mode used for the simulations presented in this work, is given in Appendix 1.A. The reader is referred to (Deck 2012; Gand and Huet 2021; Deck et al. 2014) for detailed descriptions of the ZDES equations.

Besides, in order to perform WMLES simulations of fully turbulent boundary layers, resolved turbulence must be injected into the incoming flow in order to initiate the resolved turbulence development. In the present work, roughness elements are introduced in the computational domain with the Immersed Boundary Condition technique in order to seed the transition at the inlet of the ZDES mode 3 area. More details can be found in Appendix 1.B.

As explained in the introduction, the unsteady flow is resolved only in the flow region containing the noise sources to limit the computational costs of the simulation, and the pressure radiated outside this region is calculated using surface integral methods, for both free-field acoustic radiation and reflected pressure radiation. For the isolated jet configuration, the pressure radiated in free field (noted  $p_1'$  in the following)  $\vec{x}$  is calculated using

the FWH surface formulation. The control surface ( $S$ ) is a conical type surface around the jet (see Sect. 4.7, Figs. 3 and 15). For the installed jet configuration, a complementary acoustic calculation is performed to take into account the presence of the plate in the sound radiation. This second calculation is carried out using the Kirchhoff method. The control surface ( $S_K$ ) is the part of the plate located outside the FWH control surface  $S$  (see Sect. 5.2 and Fig. 32). The calculation is performed starting from the incident pressure and its gradient provided on  $S_K$  by the free-field calculation. The resulting pressure (noted  $p_{II}'$  in the following) is added the free-field radiation  $p_I'$ . The expressions of  $p_I'$  and  $p_{II}'$  are detailed in Appendix 1.C.

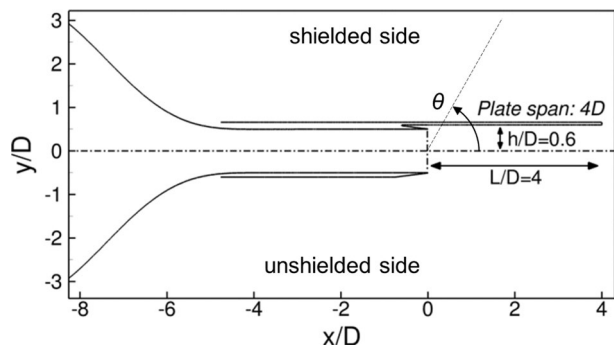
### 3 Test Cases and Simulation Setup

#### 3.1 Isolated and Installed Jet Test Cases

The jet configuration investigated in this report is a single stream, subsonic, isothermal jet from Pprime laboratory in Poitiers, France (Brès et al. 2018). The exhaust Mach number is equal to  $M=0.9$ , the nozzle exit diameter is  $D=0.05$  m, the nozzle pressure ratio is  $P_i/P_0=1.7$  and the nozzle temperature ratio is  $T_i/T_0=1.15$ , where index  $i$  corresponds to stagnation quantities at nozzle inlet and index  $0$  to static quantities in the ambient medium. The Reynolds number based on the diameter is equal to  $Re_D=10^6$  and the boundary layer inside the nozzle is tripped, so that the flow is fully turbulent. All isolated experimental data and nozzle geometry are available online (Brès et al. 2018). For the installed jet case illustrated in Fig. 1, it is chosen to locate the plate at its closest radial position with respect to the nozzle,  $0.6D$ . The distance from the nozzle exit to the plate trailing edge is  $4D$  and the wing span is  $15D$ . The experimental setup is detailed in (Piantanida et al. 2016).

Acoustic levels are analyzed on the experimental, azimuthal antenna of 18 evenly distributed microphones of Pprime (Piantanida et al. 2016). The circular antenna is centered on the jet axis with a radius of  $14.3D$  and is moved axially from  $x/D=39.29$  to  $x/D=-8.26$  ( $x/D=-1.25$  experimentally), corresponding to observation angles  $\theta$  varying from  $20^\circ$  to  $120^\circ$  (resp.  $95^\circ$ ) with a  $5^\circ$  step, as illustrated in Fig. 2. For the installed case, pressure levels are expected to depend on the azimuthal angle of the microphones  $\Phi$ , whose definition is illustrated in Fig. 2. (b). It is measured clockwise with respect to the positive  $x$  axis.  $\Phi=0^\circ$  is aligned with the positive  $z$  axis, so that angles  $0^\circ \leq \Phi \leq 180^\circ$  correspond to

Fig. 1 Jet/plate installation setup



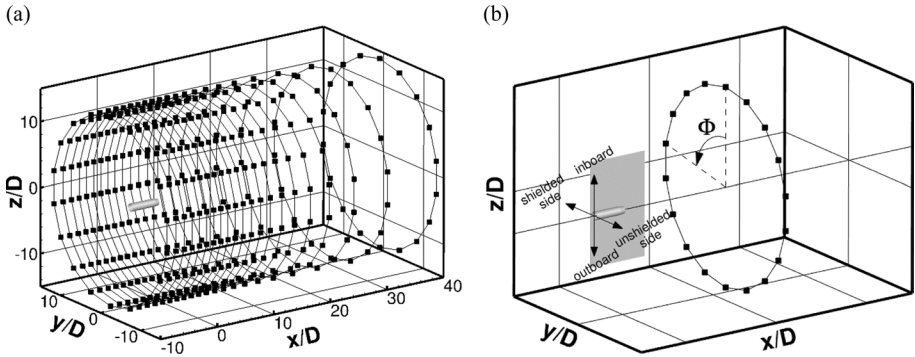
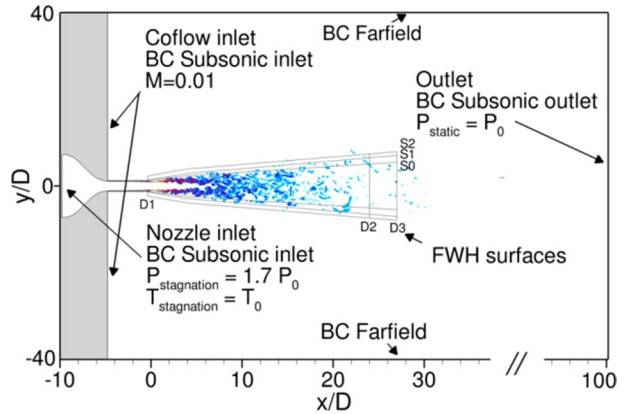


**Fig. 2** **a** Microphones positions for the different locations of the azimuthal antenna, **b** azimuthal description of the microphones on the antenna

**Fig. 3** Computational domain



positions above the flat plate (shielded side) whereas angles  $180^\circ \leq \Phi \leq 360^\circ$  are located below the plate (unshielded side).

Concerning the pressure data at the microphones, both experimental and numerical power spectral densities and integrated levels follow the  $1/M_j^4$  scaling proposed by Brès et al. (see Eq. B 8 of (Brès et al. 2018)) and the frequency range considered for the integrated levels is  $0.05 \leq St \leq 10$ .

### 3.2 Numerical Settings

The computational domain used is the same for all simulations and is illustrated for the isolated case in Fig. 3. It is similar to the one used in previous work (Gand and Huet 2021), grid stretching is applied outside the jet near-field (see meshes sizes details in Sect. 3.3) in order to damp the acoustic waves and avoid their reflections on the boundary conditions. Note that the flow inside the nozzle is computed in the simulations, including the nozzle convergent.

The CFD simulations are performed with the elsA software (Cambier et al. 2013). The spatial discretization is 2nd order accurate and relies on a 1-exact flux reconstruction at cell interfaces. The fluxes are computed with a 2nd order Roe scheme. The gradients are

computed with a Green-Gauss approach. The time integration is performed with a 2nd order accurate implicit backward differencing scheme with a timestep of  $1 \mu\text{s}$  and 5 inner sub-iterations per timestep to ensure a decrease of at least 1 order of magnitude of the residuals during the sub-iteration process.

The turbulence modelling approach used is the Zonal Detached Eddy Simulation (ZDES) (Deck 2012) which combines ZDES mode 3 (Deck et al. 2018, 2014) to achieve a Wall Modelled LES resolution in the nozzle boundary layer and ZDES mode 2 (2020) (Deck and Renard 2019) to achieve a LES resolution in the jet and a RANS modelling everywhere else as depicted in Fig. 4. In particular, the turbulence generation in the nozzle boundary layer is performed using tripping dots included in the computational domain using Immersed Boundary Conditions (IBC) as illustrated in Fig. 4. The efficiency of this method to quickly develop three-dimensional turbulence without generating spurious noise (a common limitation of synthetic turbulence generators which can be used as an alternative to the present method) is demonstrated in (Deck et al. 2018; Gand and Huet 2021), where a detailed discussion on the choice of the tripping dots parameters can be found. In the present case, the height of the tripping dots is equal to 0.6 times the local boundary layer thickness as suggested in (Deck et al. 2018).

Isolated jet simulations are first run for  $300 D/U_j$  (with  $U_j$  the jet exhaust velocity) to flush out the initial transient, after what flow statistics and data extraction for the far-field noise post-processing are computed for  $300 D/U_j$  to investigate grid convergence. As a matter of fact, the investigations carried out in Sects. 4.6 and 4.7.2 show that the choice of  $300 D/U_j$  is acceptable insofar as the data is azimuthally averaged. For the installed jet, where data cannot be azimuthally averaged, post-transient jet flow simulation is extended to  $600 D/U_j$  to reach statistical convergence.

### 3.3 Meshes

In order to improve the accuracy of the simulations, especially at high frequencies, the present simulations make use of unstructured grids to cluster the grid points in the jet shear layer near the nozzle exit where acoustic sources responsible for high frequency noise are generated. Besides, previous work showed the limitations of the structured grid approach for complex configurations (Gand and Huet 2021; Gand et al. 2017) for which unstructured grids are better suited (Zhu et al. 2018; Fosso Pouangué et al. 2015). Of interest, the present meshes rely on prisms and hexahedra near the wall, and pyramids and tetrahedra everywhere else as illustrated in Fig. 5.

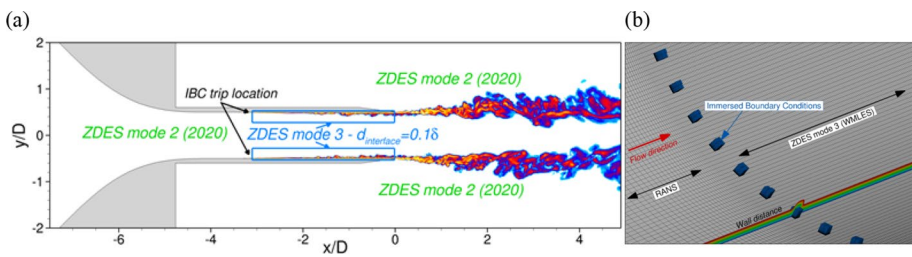


**Fig. 4** **a** ZDES modes definition, **b** illustration of the IBC trips to trigger turbulent transition inside the nozzle



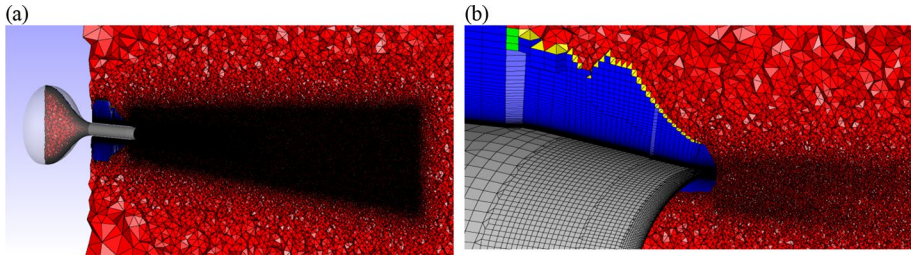


**Fig. 5** Visualizations of the unstructured mesh topology. Blue: prisms and hexahedra, yellow: pyramids, red: tetrahedral. **a** general view, **b** detail at nozzle exit

First, the focus is put on the tuning of the mesh inside the nozzle to correctly reproduce the nozzle turbulent boundary layer. Indeed, it was shown in various papers that the state of the nozzle exit boundary layer is key to jet noise generation mechanisms (Brès et al. 2018; Gand and Huet 2021; Bogey and Bailly 2005; Bogey and Marsden 2016; Bogey and Sabatini 2019). Therefore preliminary simulations are carried out with a coarse mesh in the jet to ensure that the turbulence modelling methodology derived for structured grids in (Gand and Huet 2021) and illustrated in Fig. 4 could be used with unstructured ones as well. Eventually, a wall mesh resolution of  $\Delta x^+ = r\Delta\theta^+ = 200$  is found to provide a fair agreement with experimental data (see Sect. 4.2). Note that this resolution is larger than the recommended values for ZDES mode 3 to reach accurate friction coefficient values on a flat plate, but is found sufficient for the purposes of initiating the jet flow development in (Gand and Huet 2021).

The mesh inside the nozzle is then kept constant for all the simulations, while the mesh density in the jet development area is investigated. The decoupling of the mesh densities in various areas of the computational domain is indeed one advantage of the unstructured grid approach. Using basic a priori knowledge of an isolated subsonic jet properties, the jet flow is decomposed into three areas depicted in Fig. 6: the shear layer development (in red), up to  $x/D=6$ , the jet plume mixing area from  $x/D=6$  to  $x/D=15$  and the acoustic propagation area enclosing the expected acoustic sources up to  $x/D=30D$ . These three areas are designed to parametrize the mesh sizes depending on the local flow physics and easily generate meshes of increasing density with only a few control parameters.

In Fig. 6,  $\Delta_1$ ,  $\Delta_2$  and  $\Delta_3$  are the target edge sizes used to generate the mesh with the Pointwise software (target edge size is  $\Delta_3$  in the acoustic propagation area). The metrics generally used to characterize the size of tetrahedral cells for CFD is the diameter of the inscribed sphere inside the cell.

Three meshes are created to assess the mesh sensitivity of the results. The cells sizes for these meshes are given in Table 1 along with the estimated maximal Strouhal

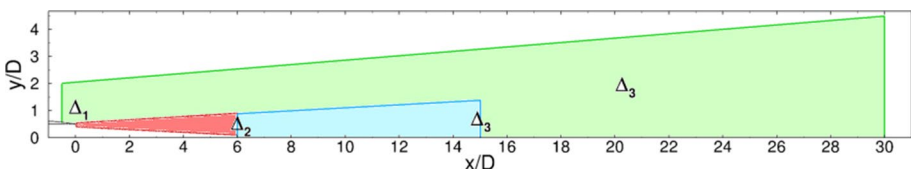


**Fig. 6** Mesh refinement areas

**Table 1** Mesh sizes (see definition of mesh refinement areas in Fig. 6)

Mesh name	Computed sizes—diameter of inscribed sphere						Mesh count (in million elements)				
	$\Delta_1/D$	$\Delta_2/D$	$\Delta_3/D$	$St_{max}(\Delta_1)$	$St_{max}(\Delta_2)$	$St_{max}(\Delta_3)$	Nozzle inlet	BL	Shear layer	Plume + farfield	Total
Uns-1	0.0021	0.015	0.027	36.0	4.9	2.8	5.5	9.3	19.2	39.8	73.8
Uns-2	0.0016	0.011	0.019	45.0	7.0	4.0	5.5	9.3	41.3	87.6	143.7
Uns-3	0.0016	0.011	0.015	45.0	7.0	4.8	11.4	9.3	41.3	119.5	181.5

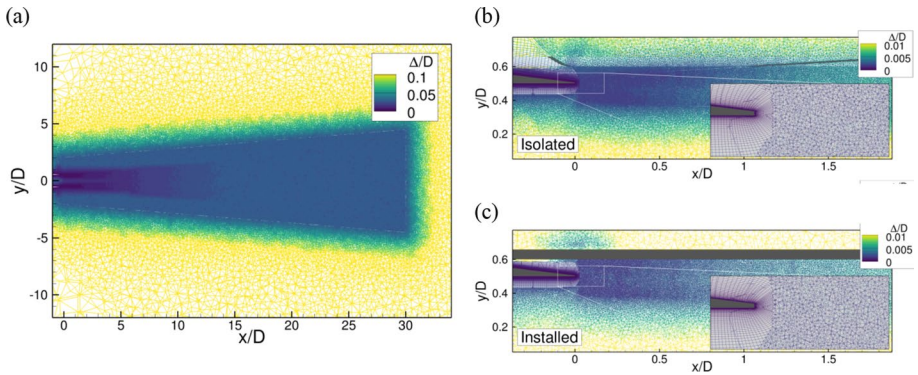


**Fig. 7** Illustration of mesh sizes for isolated and installed jet mesh "Uns-1". **a** global view, **b** detailed view, isolated configuration, **c** detailed view, installed configuration

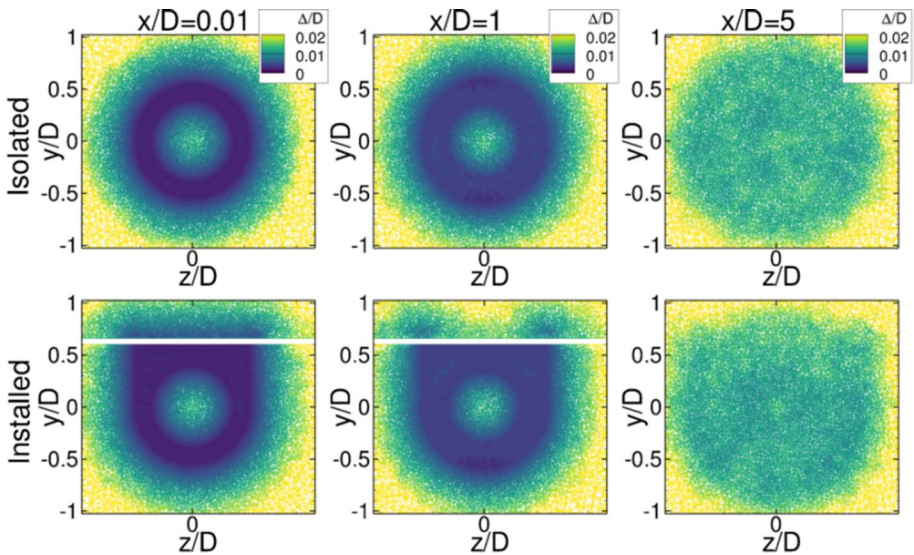


**Fig. 8** Illustration of mesh sizes in transverse planes for isolated and installed jet mesh "Uns-1"

number which can be reached assuming 15 points per acoustic wavelength, a usual criteria used for standard second-order schemes (Sagaut et al. 2006; Pont et al. 2017).

The rationale for the meshes generation is the following. A first mesh of moderate size, named "Uns-1", is created using lessons learnt from the literature and previous simulations with structured grids. The same mesh distribution and cell sizes were used to generate the installed jet mesh. Both isolated and installed jet meshes are illustrated in Figs. 7 and 8. The mesh density was then increased in order to perform a mesh sensitivity study for the isolated jet. The second mesh, "Uns-2", is derived by reducing the cell size of 20% at the nozzle lip and potential core and 30% everywhere else, resulting in a total grid count twice as large as the one of "Uns-1". Finally, mesh "Uns-3"

refinement focuses on the acoustic propagation area (in green in Fig. 6) with a reduction of 20% of the cell size compared to mesh Uns-2 in this area. Results from simulations on meshes Uns-1 and Uns-2 lead to shorten the refined area at  $x/D=27$  in this mesh to save some computational cost. The cell size is also reduced in the potential core in Uns-3 to assess the sensitivity of the results to this parameter.

The cell sizes distribution in the jet plume can be observed in Figs. 7 and 8 for the first mesh used (Uns-1). More quantitatively, the cell sizes are plotted in Fig. 9 in order to assess the differences between each mesh.

Of interest, the grid point distribution and grid sizes of structured grids used in previous studies (Gand and Huet 2021) are also plotted in Fig. 9 as references. Grid “Struct-Grid1BL” has 54 million cells, and “Struct-Grid2BL” has 156 million cells. These grids provide a discretization in the shear layer such that around 50 points are clustered in the initial shear layer vorticity thickness in the radial direction, following standard recommendations for eddy-resolving approaches (Sagaut et al. 2006) (note that a similar resolution is achieved with the unstructured meshes). It is noteworthy that due to total grid count limitations, the streamwise grid spacing for the structured grids is much larger than the one obtained with unstructured grids. The azimuthal resolution near the nozzle exit ( $\Delta_\theta/D$  and  $r\Delta_\theta/D$ , for unstructured and structured grids respectively) is also improved with unstructured grids as expected. Indeed, the equivalent grid points number near the nozzle exit is 1500 for mesh Uns-1 and 2000 for mesh Uns-2 and Uns-3 instead of 500 for the structured grid Grid2BL. It is noteworthy that several techniques can be used to try and refine locally structured grids, such as partially matching block joins, fully non conformal block interfaces or overset grids. However, in the framework of scale-resolving simulations, these approaches can induce a low-pass filtering of the solution which would be detrimental. Special care must be taken to ensure a continuity of the grid density on both sides of the blocks interfaces, which reduces the efficiency of these approaches in reducing the total grid count. Regarding the overset approach, this aspect is addressed in (Gand and Brunet 2012; Gand 2013). Without the use of such specific refinement techniques, one can estimate that the size of a structured grid with a grid density in the jet area in the radial, streamwise and azimuthal directions similar to the ones of mesh Uns-3 would be much more than 1 billion points due to the constraints

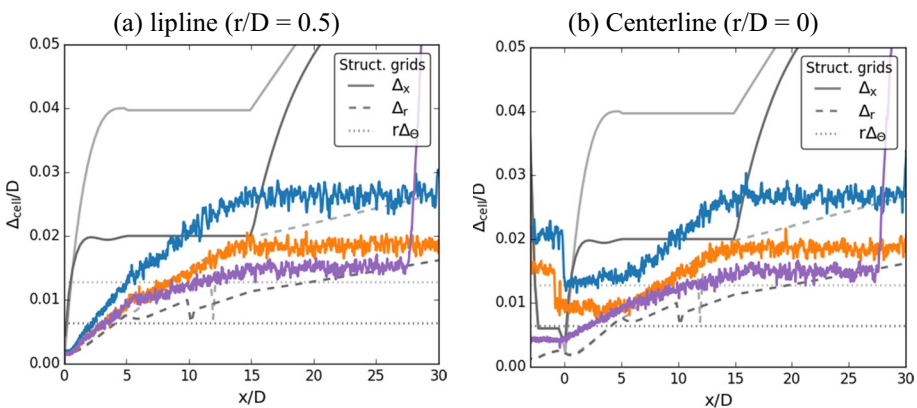


**Fig. 9** Mesh sizes along the lipline (left) and jet centerline (right). Light gray line Struct-Grid1BL, gray line Struct-Grid2BL, blue line Iso-Uns1, orange line Iso-Uns2, purple line Iso-Uns3

of the structured grid approach where local grid refinements propagate throughout the computational domain.

## 4 Validation of the Numerical Approach for an Isolated Jet

In the present section, the results of the simulations performed with the unstructured meshes (simulations with mesh “Uns-N” ( $N=1, 2, 3$ ) are named “ZDES3 MeshN”) are compared with experimental data and the simulation data of Brès et al. (Brès et al. 2018), labelled as “WMLES Brès et al. (16 M)”. It is reminded that this simulation was performed with the solver Charles of Cascade Technologies on an unstructured hexahedral mesh created by an adaptive refinement technique, using a Wall Modelled approach, a blended upwind/central 2nd order spatial scheme and a 3rd order explicit temporal integration scheme (Brès et al. 2018). For the aerodynamic part, the results of the simulation performed with a structured grid of  $156 \cdot 10^6$  cells are also included in order to illustrate the improvements achieved. Details for the simulation with the structured grid, named “ZDES3 Grid 2 (elsA-S)” in the following, can be found in (Gand and Huet 2021). It is noteworthy that this simulation was run with the same turbulence modelling approach (ZDES mode 3 in the nozzle and ZDES mode 2 everywhere else) and the same time integration scheme as the simulations with the unstructured grids but with a different spatial discretization scheme, namely a modified AUSM+P spatial scheme (Mary and Sagaut 2002).

### 4.1 Flow visualizations

Snapshots of the simulations are shown in Fig. 10. The contours of vorticity emphasize the size as well as the strength of the resolved turbulent structures, and the density gradient in the background characterizes the acoustic waves propagation. When the unstructured mesh density increases, some smaller scales seem to be captured in the aft part of the jet, around 6–8 D. However, even smaller eddies are resolved with the structured grid, which is partly attributed to the low dissipation spatial scheme used. One can also note that the propagation of acoustic waves inside the nozzle is more visible in the structured grid simulation. This is attributed to the small streamwise grid spacing in this area inherited from the

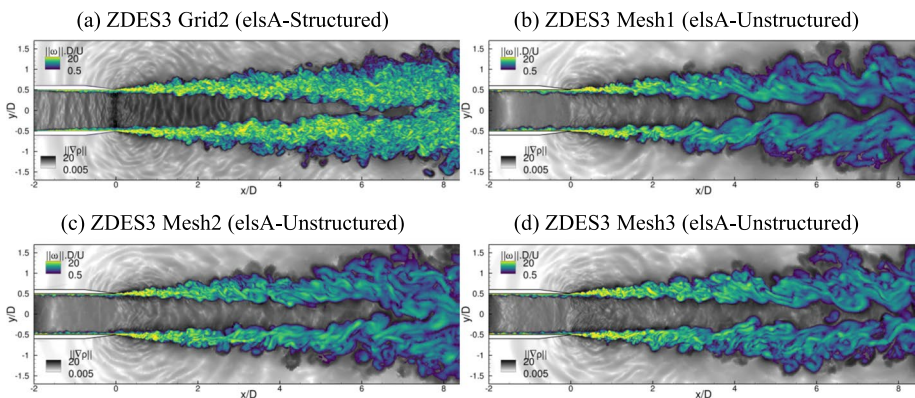


**Fig. 10** Snapshots of mean vorticity (colors) and density gradient (grayscale)

structured grid constraints to discretize the turbulence tripped in the boundary layer in the structured grid, which is not the case with the unstructured meshes. The increased mesh density in the nozzle centerline for mesh Uns-3 (see Fig. 9) seems to slightly improve this aspect.

## 4.2 Nozzle Exit Boundary Layer

Prior to analyzing the jet flow development in the simulations, the nozzle boundary layer evolution is first investigated. A turbulent boundary layer is developed downstream of the tripping dots described in section Appendix 1.B (see also a detailed analysis in (Gand and Huet 2021)). The nozzle exit boundary layer profiles are plotted in Fig. 11. The unstructured grid simulations results are in close agreement with the structured grid simulation. The experimental mean and RMS streamwise velocity profiles are fairly well reproduced and the data is close to the reference simulation of Brès et al. (Brès et al. 2018) Although the agreement is not perfect, the boundary layer obtained in the simulations is arguably representative of the experimental one in terms of thickness and three-dimensional resolved turbulence, which is conjectured to be sufficient in the frame of the present study since the objective is to initiate the jet flow development with a fully turbulent boundary layer as in the experiments.

## 4.3 Shear layer Development

In order to assess the development of the shear layer downstream of the nozzle exit, profiles along the lipline  $r/D=0.5$  are plotted in Fig. 12. The slope of the mean velocity decay is well reproduced by all simulations with unstructured meshes, with a slightly even better agreement for ZDES3 Mesh2 and ZDES3 Mesh3 which provide virtually the same results. The level of resolved fluctuations is also in good agreement with the experiments, and the mesh sensitivity is also not significant for this quantity.

The improvement of the unstructured mesh simulations over the structured one is obvious. It is conjectured that the mesh spacing in the streamwise direction was too large compared to the spacing in the other directions in the structured grid due to total grid count limitation (see grid sizes in Fig. 9). The inappropriate aspect ratio of the cells appears to impair the overall development of the jet for  $0 < x/D < 10$ . This appears to result in an underestimation of the RMS velocity in the shear layer and a global imbalance within the

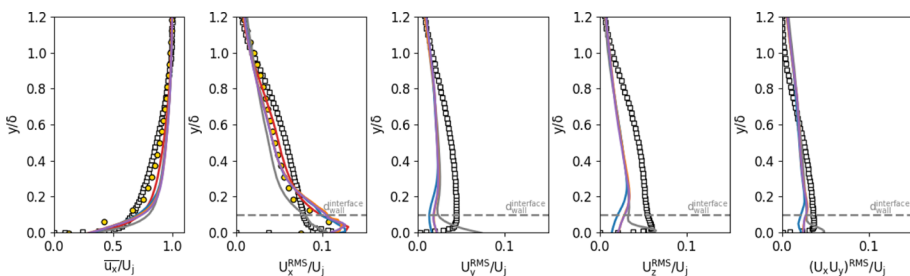
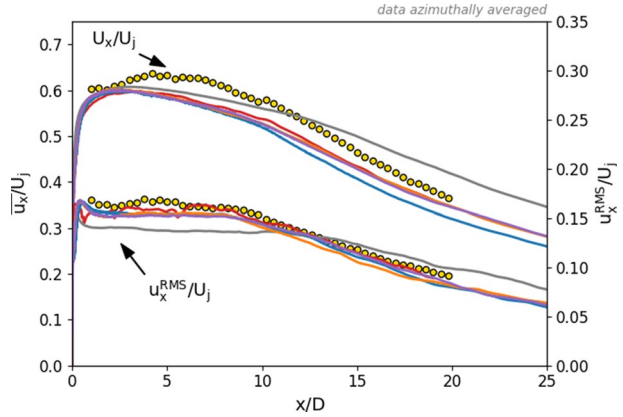


**Fig. 11** Nozzle exit boundary layer profiles (azimuthally averaged). The horizontal dashed line on the right hand side plots represents the location of the RANS/LES interface used for the ZDES mode 3 modelling.  $\square$  DNS Sillero et al., yellow circle Exp. Pprime, red line WMLES Brès et al. (16 M), gray line ZDES3 Grid2 (elsA-S), blue line ZDES Mesh1, orange line ZDES mesh 2, purple line ZDES mesh 3

**Fig. 12** Mean and RMS streamwise velocity along the jetlipline ( $r/D=0.5$ ) (azimuthally averaged). Yellow circle Exp. Pprime, Red line WMLES Brès et al. (16 M), gray line ZDES3 Grid2 (elsA-S), blue line ZDES Mesh1, orange line ZDES mesh 2, purple line ZDES mesh 3



simulated jet which do not present the correct decay slopes for  $x/D > 10$  for the mean and RMS velocities. In this regard, it is assumed that the smaller size and isotropy of the grid cells of the unstructured grids provide a better discretization of the shear layer.

The streamwise evolution of the shear-layer momentum thickness  $\delta_\theta$  is presented in Fig. 13. It is computed as suggested in (Brès et al. 2018):  $\delta_\theta = \int_0^{r_{0.05}} \frac{u_x(x,r)}{u_x(x,0)} \left( 1 - \frac{u_x(x,r)}{u_x(x,0)} \right) dr$  where  $u_x(x, r)$  is the time- and azimuth-averaged streamwise velocity and  $r_{0.05}$  accounts for the co-flow and is the distance where  $u_x(x, r_{0.05}) - U_0 = 0.05u_x(x, r_{0.05})$  ( $U_0$  being the co-flow velocity). The simulations with the unstructured meshes predict the correct slope of the streamwise variation of  $\delta_\theta$ , conversely to the simulation with the structured grid which underestimates the shear layer growth rate for  $x/D > 2$ .

### 4.4 Jet Flow Development

Mean and RMS streamwise velocity profiles along the jet centerline ( $r/D=0$ ) shown in Fig. 14 are consistent with the previous comments. All three simulations performed with unstructured meshes are in very good agreement with the reference data. The mesh

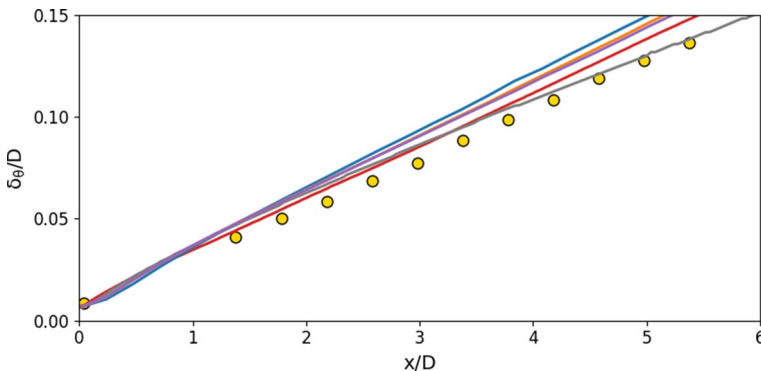


**Fig. 13** Shear layer momentum thickness  $\delta_\theta$  (azimuthally averaged). Yellow circle Exp. Pprime, red line WMLES Brès et al. (16 M), gray line ZDES3 Grid2 (elsA-S), blue line ZDES Mesh1, orange line ZDES mesh 2, purple line ZDES mesh 3

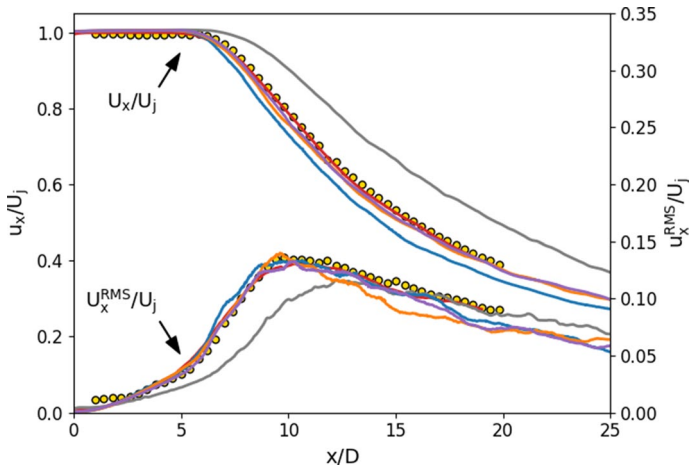


**Fig. 14** Mean and RMS velocities along the jet centerline. Yellow circle Exp. Pprime, red line WMLES Brès et al. (16 M), gray line ZDES3 Grid2 (elsA-S), blue line ZDES Mesh1, orange line ZDES mesh 2, purple line ZDES mesh 3

sensitivity of the results is likely to stem from the total simulation time rather than from a “true” mesh effect since no azimuthal average can be performed at this location and the second order statistics may not be completely converged with  $300 D/U_j$  as investigated in Sect. 4.6 (see Fig. 18).

Again, the simulation methodology using unstructured meshes brings about a significant improvement over our previous results with structured grids which failed to predict the jet potential core length. As explained for the shear layer development in the previous section, this seems to be a consequence of the large aspect ratio cells in the structured grid (elongated in the streamwise direction due to total grid count limitations) which might cause an imbalance between the generation and discretization of large energy producing turbulent structures and small dissipating eddies. This is also illustrated by the flow visualizations in Fig. 10 which show that the structured mesh solution appears to be biased with a slower – but unphysical – jet development probably associated with the persistence of the smallest structures visualized.

#### 4.5 Near Field Pressure Fluctuations Spectra

In the experiments (Brès et al. 2018), the jet near pressure field is measured with microphones mounted on a so-called “cage array”, which locations are depicted in Fig. 15. Pressure spectra at these locations presented in Fig. 16 provide first insights on the acoustics predicted by the simulations. For each simulation, the PSD was computed using the Welch method with 30 blocks, 50% overlap and a Hanning window from the signals extracted at each solver iteration ( $\Delta t = 10^{-6}$  s).

In line with the previous sections, the unstructured meshes simulations predict the experimental spectra with a good accuracy up to  $St_D = 3$  for the most upstream locations and  $St_D = 1$  for the most downstream one. However, in all cases the energy peak/hump is located at frequencies around  $St_D = 0.3$ . Therefore it seems that most noise sources are fairly well captured by the simulations. Of interest, one can see in Fig. 15 that the extraction



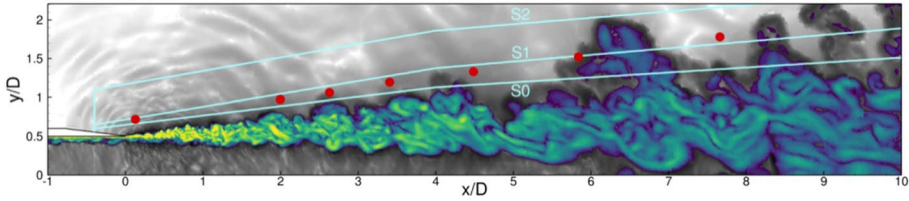


**Fig. 15** Location of the jet near field probes (red dots, "microphones cage array" in the experiments Brès et al. 2018) and extraction surfaces (S0, S1, S2) for the far-field noise post-processing

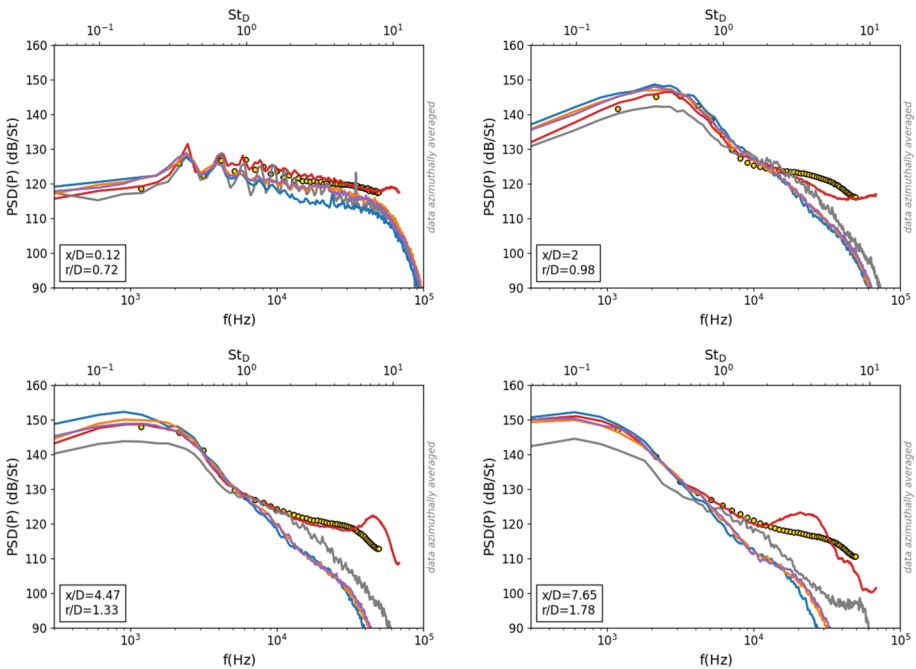


**Fig. 16** Pressure fluctuations spectra in the jet near-field (azimuthally averaged). Yellow circle Exp. Pprime, red line WMLES Brès et al. (16 M), gray line ZDES3 Grid2 (elsA-S), blue line ZDES Mesh1, orange line ZDES mesh 2, purple line ZDES mesh 3

surface S0 is closer to the jet than the cage array probes, which was done on purpose to mitigate the acoustic waves dissipation by the mesh in order to improve the accuracy of the far-field noise prediction at higher frequencies.

#### 4.6 Statistical Convergence of the Flow Data

A total simulation time of  $300 D/U_j$  is typically used in the literature as well as in the previous section for this type of isolated jets, but some papers indicate that this may be insufficient to reach statistical convergence, including the reference paper of Brès et al. (2018) for the present test case. For industrial cases, flow averages are often computed over with

100  $D/U_j$  time samples due to computational costs. Furthermore, it is common to use an azimuthal average to compensate for the short simulation time, but this is obviously not possible for installed cases.

Therefore, the simulation with the mesh “Uns-3” was run for a total of 2100  $D/U_j$  in order to assess the convergence of the computation of the flow statistics and spectra and provide some insights on the best practices required for the simulation of installed cases. The results presented in this section involve both the influence of the cumulated total simulation time from 100  $D/U_j$  up to 2100  $D/U_j$  and the results obtained for samples of 100  $D/U_j$  and 300  $D/U_j$  in order to assess the repeatability of the results when using such short time samples for the computation of the flow statistics.

The influence of the total simulation time and azimuthal average on the shear layer development is evidenced in Fig. 17. The azimuthally averaged profiles are almost converged with 100  $D/U_j$ , with only small variations among the 100  $D/U_j$  samples for  $x/D > 15$ . On the other hand, the raw profiles in the  $z=0$  plane shown on the right hand side of Fig. 17 display more significant discrepancies between the 100  $D/U_j$  and even 300  $D/U_j$  samples at all streamwise locations, and it seems that a total simulation time of at least 600  $D/U_j$  is necessary to reach consistent results.

The profiles of mean and RMS streamwise velocity along the jet axis plotted in Fig. 18 are in line with the previous comments. Of interest, the dispersion of the results obtained with 100  $D/U_j$  and 300  $D/U_j$  samples is quite significant for quantitative comparisons but would not lead to misinterpretation of the simulation results.

The near-field pressure spectra shown in Fig. 19 provide first insights on the influence of the total simulation time on the noise predictions. The dispersion of the results from 300  $D/U_j$  samples at low frequencies ( $St < 0.15$ ) is of the order of 2 dB/St and reaches around 5 dB/St for 100  $D/U_j$  samples, but the spectra seem to collapse for  $T \geq 600 D/U_j$ . However, when azimuthally averaged (left part of the figures), the results from 300  $D/U_j$  appear fairly well converged.

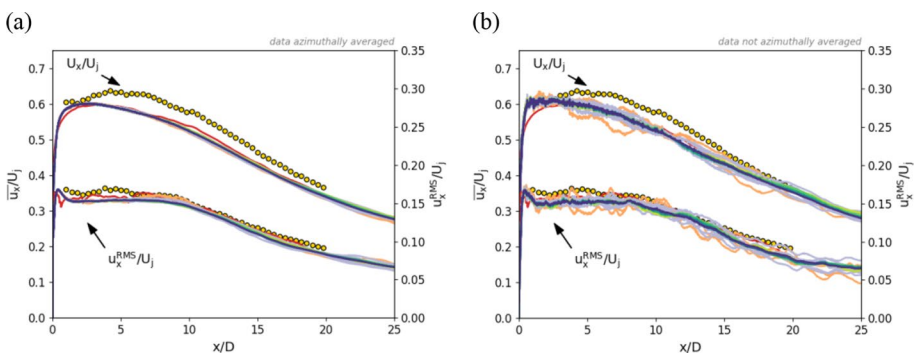


**Fig. 17** Profiles of mean and RMS streamwise velocity along the jet lipline ( $r/D=0.5$ ). **a** with azimuthal averaging, **b** no azimuthal averaging. Yellow circle Exp. Pprime, red line WMLES Brès et al. (16 M), orange line ZDES3 Mesh3 –  $T=100D/U_j$  samples, light gray line ZDES3 Mesh3 –  $T=300D/U_j$  samples, light green line ZDES3 Mesh3 –  $T=600D/U_j$ , green line ZDES3 Mesh3 –  $T=900D/U_j$ , dark green line ZDES3 Mesh3 –  $T=1200D/U_j$ , light blue line ZDES3 Mesh3 –  $T=1500D/U_j$ , blue line ZDES3 Mesh3 –  $T=1800D/U_j$ , purple line ZDES3 Mesh3 –  $T=2100D/U_j$

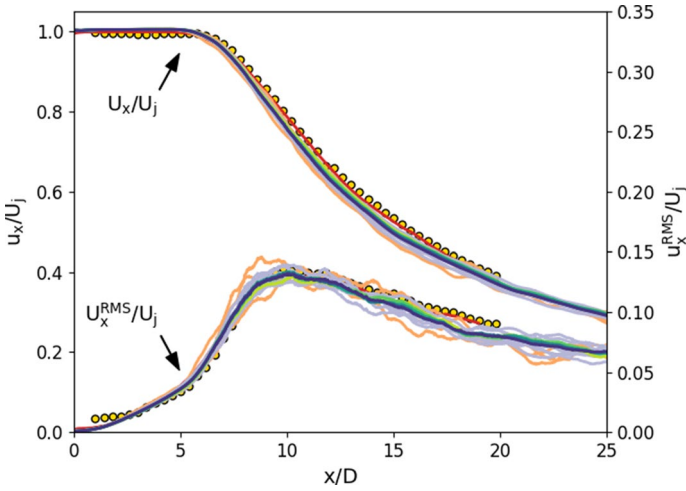


**Fig. 18** Profiles of mean and RMS streamwise velocity along the jet axis. Yellow circle Exp. Pprime, red line WMLES Brès et al. (16 M), orange line ZDES3 Mesh3 –  $T = 100D/U_j$  samples, light purple line ZDES3 Mesh3 –  $T = 300D/U_j$  samples, light green line ZDES3 Mesh3 –  $T = 600D/U_j$ , green line ZDES3 Mesh3 –  $T = 900D/U_j$ , dark green line ZDES3 Mesh3 –  $T = 1200D/U_j$ , light blue line ZDES3 Mesh3 –  $T = 1500D/U_j$ , blue line ZDES3 Mesh3 –  $T = 1800D/U_j$ , purple line ZDES3 Mesh3 –  $T = 2100D/U_j$

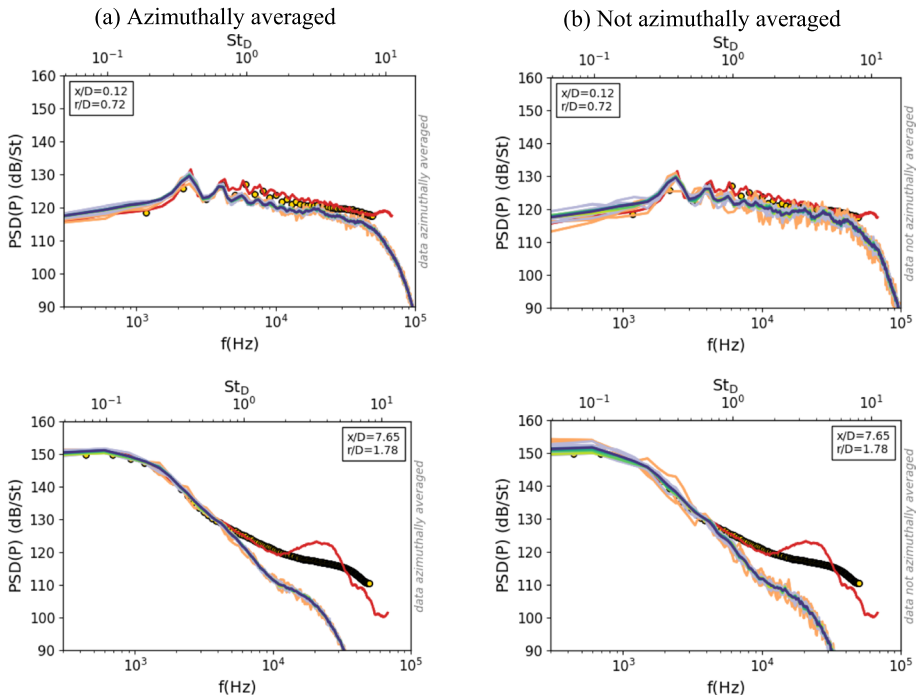


**Fig. 19** Pressure fluctuations spectra in the jet near-field. Yellow circle Exp. Pprime, red line WMLES Brès et al. (16 M), orange line ZDES3 Mesh3 –  $T = 100D/U_j$  samples, light purple line ZDES3 Mesh3 –  $T = 300D/U_j$  samples, light green line ZDES3 Mesh3 –  $T = 600D/U_j$ , green line ZDES3 Mesh3 –  $T = 900D/U_j$ , dark green line ZDES3 Mesh3 –  $T = 1200D/U_j$ , light blue line ZDES3 Mesh3 –  $T = 1500D/U_j$ , blue line ZDES3 Mesh3 –  $T = 1800D/U_j$ , purple line ZDES3 Mesh3 –  $T = 2100D/U_j$

## 4.7 Noise Radiation Sensitivity Study

The extrapolation of the pressure fluctuations to the observer positions is performed with the FWH integral surface formulation detailed in Appendix 1.C. Unsteady flow data are stored on the surface every two iterations of the aerodynamic simulation (frequency sampling  $f_s = 500,000$  Hz). This limited downsampling, together with the second order time scheme of the flow simulation, ensure the data stored are not aliased in time.

The radiation surface needs to be located far enough from the jet to enclose all the noise sources, but the farther the surface the higher the numerical dissipation of the acoustic waves in the CFD simulation before reaching the surface. Hence, its location must be determined very carefully to take into account all the noise sources and to provide the minimum numerical attenuation of the high frequency levels. Three different lateral surfaces, S0, S1, and S2 and two axial extents with endcaps D2 and D3 (see Figs. 3 and 15) are considered. For the sake of generality, the nodes of the radiation surfaces do not correspond to nodes of the CFD mesh and unsteady flow fields are projected on these surfaces using a second-order accurate interpolation. To avoid spatial aliasing, the surface grids density is similar to the volume one.

### 4.7.1 Position of the Porous Surface and CFD Grid Density

The noise radiated to the far-field from surfaces with different lateral positions and axial extents is illustrated in Fig. 20. First, the three acoustic simulations S0-D1-D3, S1-D1-D3 and S2-D1-D3 collapse in the low-frequency range, the surfaces therefore enclose the dominant noise sources. The farther away the surface is from the jet plume, the higher the dissipation of the high frequencies: for instance, the level difference between S0-S1-D3 and S2-D1-D3 is 0.3 dB for  $St=0.5$ , 1.5 dB for  $St=1$  and 5.1 dB for  $St=2$ . Second, the axial extent of the surface is clearly sufficient to capture the noise sources and no difference is observed when the surface is closed with D2 ( $x/D=24$ ) or D3 ( $x/D=27$ ). The most energetic frequencies being well resolved for all the surfaces considered, integrated pressure levels are very similar for the four simulations. At  $30^\circ$ , the maximum difference is 0.2 dB. As the contribution of the high frequencies increases with increasing observation angle, this discrepancy rises to 1.4 dB at  $90^\circ$ . The surface S0-D1-D2 is used in the rest of the analyses of the isolated jet.

The density of the aerodynamic numerical grid on noise levels is investigated in Fig. 21, where noise radiation results obtained with ZDES Mesh1, Mesh2 and Mesh3 are

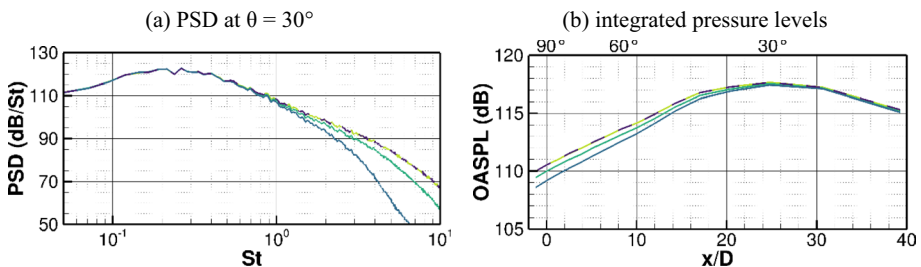


**Fig. 20** Simulated far-field pressure levels from different porous surfaces (ZDES Mesh3). Light green line S0-D1-D3, green line S1-D1-D3, light blue line S2-D1-D3, purple line S0-D1-D2

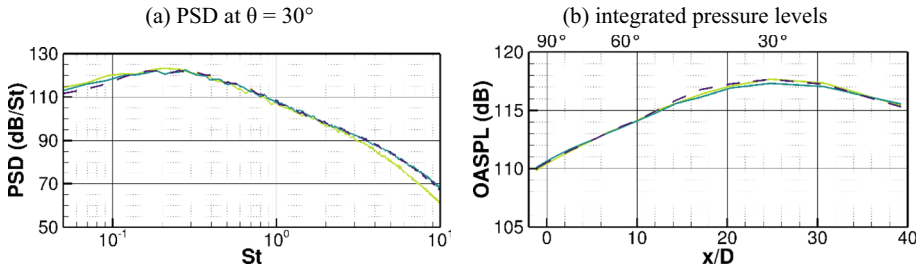


**Fig. 21** Simulated far-field pressure levels from different CFD meshes (surface S0-D1-D2). Light green line ZDES Mesh1, light blue line ZDES Mesh2, purple line ZDES Mesh3

illustrated. The pressure spectral densities, Fig. 21a, are very similar up to  $St=2$ , the three numerical grids are therefore sufficient to capture the low- and medium-frequency noise of the jet (the differences observed between the different meshes in the low frequency part of the spectra come from the insufficient statistical convergence, as discussed later in Sect. 4.7.2). For larger frequencies, the pressure levels are lower with Mesh1 whereas Mesh2 and Mesh3 provide similar levels up to the maximum considered frequency,  $St=10$ . This observation is in line with the near-field spectra presented in Sect. 4.5. The identical results obtained with Mesh2 and Mesh3 indicate the grid refinement does not improve the propagation of the acoustic waves up to the storage surface. The most energetic noise levels lying below  $St=1$ , the high-frequency numerical dissipation observed with Mesh1 has no significant influence on the integrated levels illustrated in Fig. 21b, where discrepancies are below 0.4 dB for all observation angles.

#### 4.7.2 Statistical Convergence of the Levels

This paragraph investigates the statistical convergence of the noise levels. The methodology is similar to the one used in Sect. 4.6 for the aerodynamic flow fields. Power spectral densities and integrated pressure levels are evaluated for different time length varying from  $100 D/U_j$  to  $2100 D/U_j$  and results are presented without and with azimuthal averaging.

Figure 22 reproduces power spectral densities at  $30^\circ$  observer position without (left) and with (right) azimuthal averaging of the levels. In the absence of azimuthal averaging, only one azimuth is considered for the reproduction of the results. The conclusions

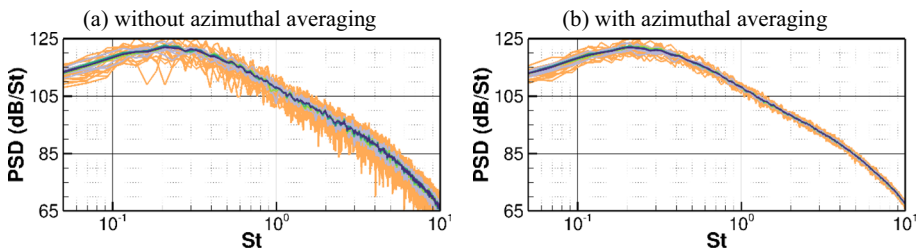


**Fig. 22** Convergence of the power spectral densities at  $30^\circ$  with the duration of the time signal. Orange line  $100 D/U_j$  samples, light purple line  $300 D/U_j$  samples, light green line  $600 D/U_j$ , green line  $900 D/U_j$ , dark green line  $1200 D/U_j$ , light blue line  $1500 D/U_j$ , blue line  $1800 D/U_j$ , purple line  $2100 D/U_j$

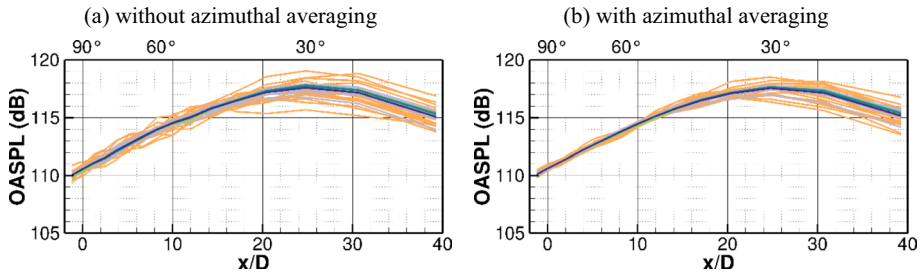
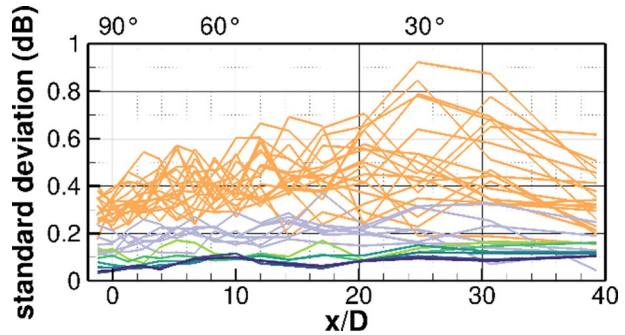


**Fig. 23** Convergence of the integrated pressure levels with the duration of the time signal. Orange line 100  $D/U_j$  samples, light purple line 300  $D/U_j$  samples, light green line 600  $D/U_j$ , green line 900  $D/U_j$ , dark green line 1200  $D/U_j$ , light blue line 1500  $D/U_j$ , blue line 1800  $D/U_j$ , purple line 2100  $D/U_j$

**Fig. 24** Standard deviation of the OASPL along the azimuthal direction. Orange line 100  $D/U_j$  samples, light purple line 300  $D/U_j$  samples, light green line 600  $D/U_j$ , green line 900  $D/U_j$ , dark green line 1200  $D/U_j$ , light blue line 1500  $D/U_j$ , blue line 1800  $D/U_j$ , purple line 2100  $D/U_j$



are qualitatively the same as for the aerodynamic data. Without azimuthal averaging, 100  $D/U_j$  and 300  $D/U_j$  samples do not provide converged spectra and the dispersion is of about 10 dB and 5 dB, respectively, for all the frequencies considered. These discrepancies vanish when the signal length increases and convergence is reached for 600  $D/U_j$ . Azimuthal averaging improves the convergence of the spectra, in particular for the high frequencies, but a dispersion of about 5 dB remains visible for low frequencies with 100  $D/U_j$  samples, and of about 2 dB for 300  $D/U_j$  samples. This is a consequence of the stronger azimuthal correlation of the low frequency noise, which reduces the efficiency of the averaging in comparison to the lower correlated, higher frequency levels (see Appendix 2). The observations are globally similar for other observation angles, not reproduced here.

The axial evolution of the integrated pressure levels is visible in Fig. 23. Without azimuthal averaging, the dispersion of the 100  $D/U_j$  samples varies between 1 dB at 90° and 4 dB at 25°. This variation reduces to a maximum of 0.5 dB for 300  $D/U_j$  samples, except for the 6th sample ( $1500 D/U_j \leq T \leq 1800 D/U_j$ ) in the downstream arc ( $x/D \geq 18$ ) where specific acoustic events lower the levels up to 1 dB. As soon as the statistics are performed over 600  $D/U_j$ , levels are converged up to 0.15 dB in the upstream arc and 0.3 dB in the downstream arc. Azimuthal averaging improves convergence for  $x/D < 20$  (observation angle below 35°) but not in the downstream arc, because of the dispersion of the low-frequency, energetic levels of the PSDs observed in Fig. 22.

To conclude these investigations, the standard deviation of the OASPL along the azimuth (root-mean-square value of the OASPL evolution along the azimuthal direction, for a given axial position) is illustrated in Fig. 24 for each axial position of the microphone antenna. In agreement with previous observations, the standard deviation slowly decreases as the length of the time signals increase. It globally varies up to 0.9 dB for 100  $D/U_j$  samples, between 0.2 and 0.3 dB for 300  $D/U_j$  samples, reduces to circa 0.15 dB for 600  $D/U_j$  and is below 0.1 dB for 2100  $D/U_j$ .

#### 4.8 Acoustic Assessment of the Simulation

To end with the isolated jet, in this section the simulated results obtained with ZDES Mesh 3, 2100 $D/U_j$  time length and azimuthal averaging are compared with the simulation of Brès et al. (2018) and experimental data.

Simulated and experimental power spectral densities are reproduced in Fig. 25. Brès et al. assume the limit frequency of their simulation is  $St \sim 2$ . Above this frequency simulated levels depart from the experimental ones and particularly exhibit a strong overestimation for the low observation angles, below  $30^\circ$ , whereas below  $St = 2$  the agreement with the experiments lies within 0.5 dB.

In the present simulation ZDES3 Mesh3, computed levels qualitatively recover the shape of the experimental spectra for all observer angles displayed. The higher grid density ( $181 \times 10^6$  elements) shifts the limit frequency to a much higher value and the agreement with the experiments remains within 5 dB for the maximum experimental frequency available,  $St = 8$ . More quantitatively, the low-frequency, most energetic levels are slightly larger than those of Brès et al., for all observer positions. At  $30^\circ$  the agreement with the experiments is very good, but the overestimation of the levels rises with the observation angle. Medium frequency levels ( $St \sim 0.2 - 0.3$ ) are overpredicted up to 3 dB at  $60^\circ$ , whereas a 2 dB overprediction is observed at  $90^\circ$  for both low and medium frequencies. This

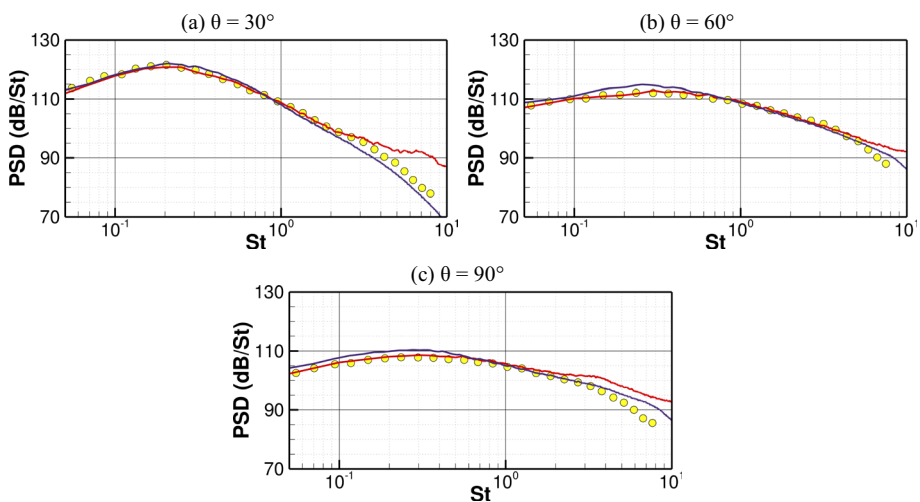


**Fig. 25** Experimental and simulated pressure spectra. Yellow circle Exp. Pprime, red line WMLES Brès et al. (16 M), purple line ZDES3 Mesh3 ( $T = 2100 D/U_j$ )

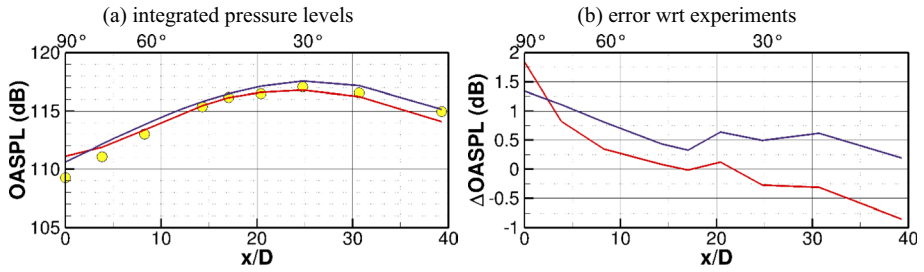


**Fig. 26** Overall sound pressure levels computed on the Strouhal bandwidth [0.05; 10]. **a** integrated pressure levels, **b** level difference between simulations and experiments. Yellow circle Exp. Pprime, red line WMLES Brès et al. (16 M), purple line ZDES3 Mesh3 ( $T = 2100 D/U_j$ )

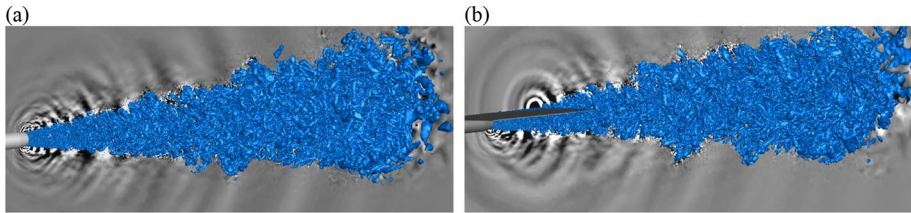


**Fig. 27** Flow visualizations. Left: isolated case, right: installed case. **a** isolated case, **b** installed case. Density gradient (grayscale) and isosurface of Q criterion (blue)  $Q \cdot D^2/U_j^2 = 2.5 \cdot 10^{-3}$

overprediction is to be associated with the one observed in the near field, see Sect. 4.5. It is related with the slight overshoot of the turbulent velocity downstream of the nozzle lip (Fig. 12), possibly corresponding to some reminiscent laminar/turbulent transition mechanisms in the early stages of the shear layer (despite the tripping of the nozzle boundary layer) which are known to be efficient noise radiators (Zaman 1985; Zaman 1985).

The consequence of the overestimation of the low- and medium-frequency levels in the PSDs is a slight overprediction of the integrated pressure levels, as illustrated in Fig. 26. In Fig. 26a, the simulation recovers the experimental noise directivity. Figure 26b reproduces the integrated level difference between the simulations and the experiments, positive values indicating an overprediction of the simulation. For both simulations, the higher the observation angle the larger the overprediction. For simulation ZDES Mesh 3, this overprediction is caused by the slight overestimation of the low- and medium-frequency levels, and it globally remains below 0.5 dB to 1 dB for most angles.

## 5 Installed Jet Configuration

Following the results of the isolated case, the installed jet simulation is performed with the grid Mesh1. This grid density is assumed to be sufficient to capture the main physical phenomena at a reasonable computational cost, in particular the scattering of turbulence by the plate trailing edge, which is important for low frequencies. In addition, the simulation is run for  $600 D/U_j$  to ensure the statistical convergence of the data, which cannot be azimuthally averaged.



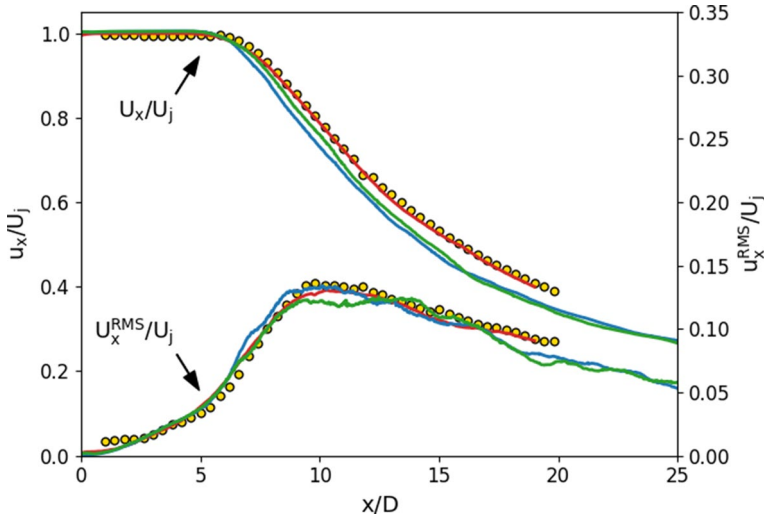


**Fig. 28** Mean and RMS of streamwise velocity along the jet centerline ( $r/D=0$ ). Yellow circle Isol. —Exp. Pprime, red line Isol. —WMLES Brès et al. (16 M), blue line Isol. —ZDES3 Mesh1, green line Inst. —ZDES3 Mesh1

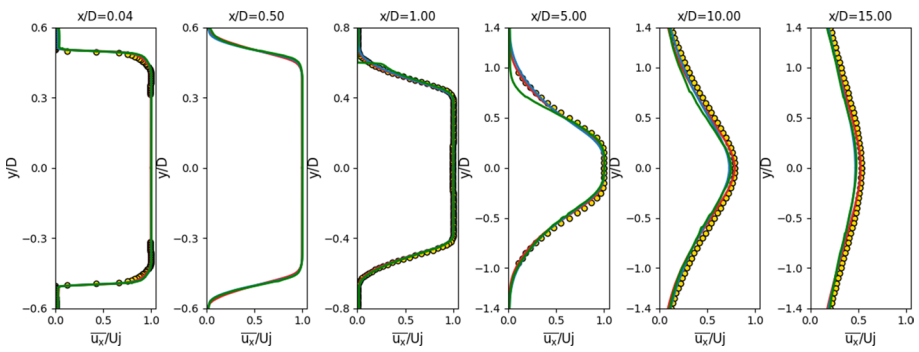


**Fig. 29** Radial profiles of streamwise velocity. Yellow circle Isol. —Exp. Pprime, red line Isol. —WMLES Brès et al. (16 M), blue line Isol. —ZDES3 Mesh1, green line Inst. —ZDES3 Mesh1

## 5.1 Flow Simulation

Instantaneous flow visualizations are shown in Fig. 27. The shielding effect above the plate as well as the pressure waves scattering by the plate trailing edge are observed in the simulation of the installed case. No obvious influence of the installation can be seen on the jet flow development, which is expected with this configuration.

The velocity profiles along the jet centerline plotted in Fig. 28 confirm that the jet flow development is not modified by the presence of the plate. The isolated and installed case simulations are in good agreement with each other and the experimental data for the isolated case (Brès et al. 2018) (which are assumed to be valid for the installed case as well).

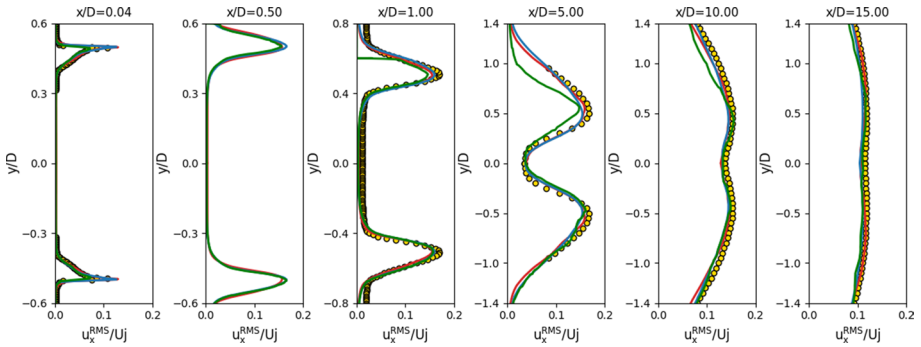


**Fig. 30** Radial profiles of RMS of streamwise velocity. Yellow circle Isol. —Exp. Pprime, red line Isol. —WMLES Brès et al. (16 M), blue line Isol. —ZDES3 Mesh1, green line Inst. —ZDES3 Mesh1

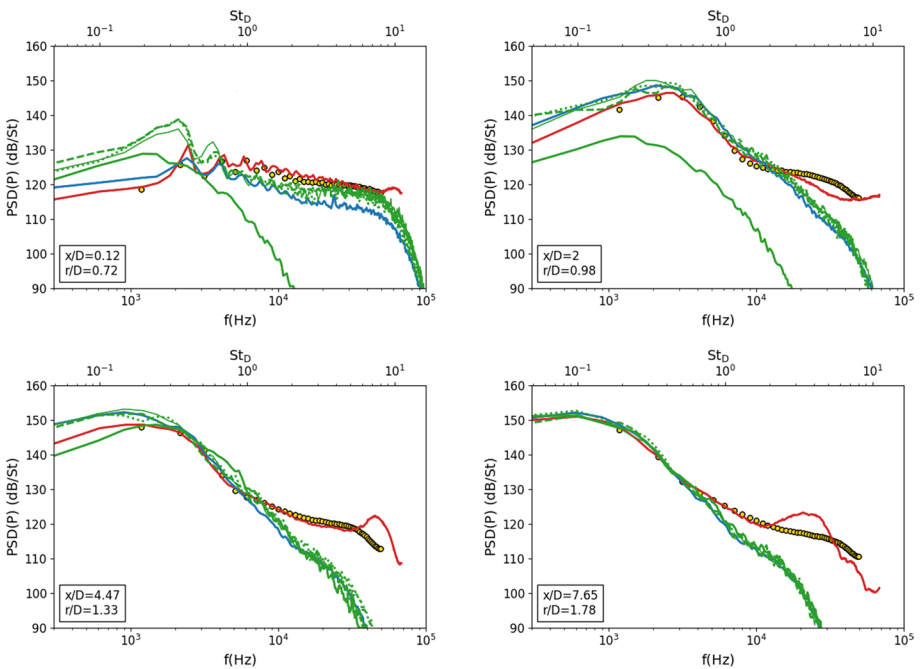


**Fig. 31** Pressure spectra in the jet near-field. Shielded position is  $\Phi = 90^\circ$ ; unshielded position is  $\Phi = 270^\circ$ ; inboard/outboard position are  $\Phi = 0^\circ/180^\circ$ . Yellow circle Isol. —Exp. Pprime, red line Isol. —WMLES Brès et al. (16 M), blue line Isol.—ZDES3 Mesh1, green line Inst. — ZDES3 Mesh1. Dark black line shielded, black line outboard, -- inboard, · · · unshielded

The radial profiles of the mean and RMS velocity (Figs. 29 and 30) show that the jet shear layer development only slightly modified in the plate wake (profiles at  $x/D = 1, 5$  and  $10$  for  $0.5 < r/D < 1$ ).

The installation effect on the jet near-field pressure fluctuations is investigated in Fig. 31. At  $x/D=0.12$ , the shielding leads to a strong reduction of medium- and high-frequency levels above the plate and strengthens the low-frequency content. This low-frequency rise is also observed for the other azimuthal positions. At  $x/D=2$ , the influence of the plate is essentially limited to the shielded observer with a 10 dB reduction compared to the isolated configuration, whereas low frequency levels increase below the wing (unshielded position). For inboard and outboard azimuthal positions, the results are very close to the simulations and the measurements of the isolated case. As the observer location moves downstream ( $x/D > 4$ ), levels start to collapse between installed and isolated jets.

## 5.2 Radiated Noise

### 5.2.1 Modeling of Noise Radiation

Compared to the isolated jet, the presence of the flat plate impacts the radiated noise in two different ways. First, due to the coupling between the jet and the plate turbulence is scattered by the trailing edge and generates additional noise (Cavaliere et al. 2014; Ffowes Williams and Hall 1970). Second, the flat plate reflects the pressure waves and act as a shielding. The classical methodology to compute such a configuration is to solve the propagation of the acoustic waves around the plate in the CFD simulation, the coupling with an integral method being performed outside of the jet-plate region in the uniform, free-field flow (Tyacke et al. 2019; Rego et al. 2020; Bondarenko et al. 2012; Angelino et al. 2018, 2019; Stich et al. 2019; Wang et al. 2020; Silva et al. 2015). Such an approach may however be very expensive, in particular when the extent of the plate is large. Here, a low-cost alternative method is proposed. In order to limit the computational time, sound propagation around the flat plate is neither included in the CFD simulation (except in the very close vicinity of the jet) nor accounted for through a CFD-CAA coupling, but modelled during the radiation process. Pressure time signals are reconstructed in a two-step simulation from the unsteady flow fields stored on a porous surface surrounding the jet. The direct radiation from the jet to the microphones is performed in a first step using the FWH formulation. The acoustic scattering by the part of the flat plate enclosed in the porous surface is computed by the CFD simulation and is therefore included in this step of the radiation process.

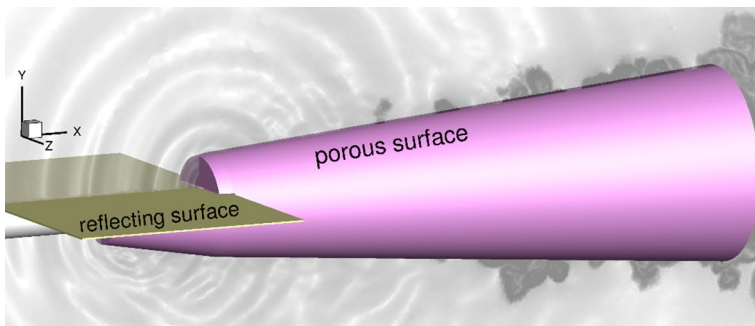


Fig. 32 Porous and reflecting surfaces used for noise radiation

Acoustic contributions on the flat plate outside of the porous surface are modelled in a second step: the pressure, its gradient and its time derivative are computed on the plate using the FWH integral formulation and reflections and shadow effects of the flat plate outside of the porous surface on the radiated noise are modelled using Kirchhoff method as presented in Appendix 1.C.

An illustration of the porous and reflecting surfaces used in the study is visible in Fig. 32. The porous surface is adapted from that of the isolated jet configuration to fit the contour of the plate and to include only the jet and the vicinity of the plate trailing edge. The validation of the noise radiation methodology is provided in Appendix 3, while the analysis of the pressure radiated on the azimuthal antenna is detailed hereafter.

### 5.2.2 Pressure on the Azimuthal Antenna

The accuracy of the installed jet simulation is now addressed through the comparison of the radiated pressure on the azimuthal antenna with the experimental data of Pprime. The pressure spectra above the plate (shielded side,  $\Phi = 80^\circ$ ) are reproduced in Fig. 33 for four positions of the axial antenna. There are no experimental data available for the observation angle  $\theta = 120^\circ$  but jet-plate interaction noise is known to be large at aft angles (Lawrence and M. A. and R. H. Self 2011; Belyaev et al. 2017; Ffowcs Williams and Hall 1970), hence the interest for its analysis. Isolated jet experimental and numerical data (Mesh 3, porous surface S0,  $T = 2100 D/U_j$ ) are also reproduced in the figure for reference and illustration of installation effect on noise. It is reminded the grid cut-off frequency is much lower for the installed jet ( $St = 1$ ) due to the coarser mesh and the porous surface located farther away from the jet. For the first three angles, we observe a good agreement between the installed simulation and the experimental data up to the grid cut-off frequency, despite a slight overestimation up to 3 dB of the low frequency levels especially at  $30^\circ$ . The pressure levels are driven by the direct contribution, reflections on the flat plate being always negligible except for the low frequencies ( $St \leq 0.1$ ) at  $90^\circ$  where they become comparable

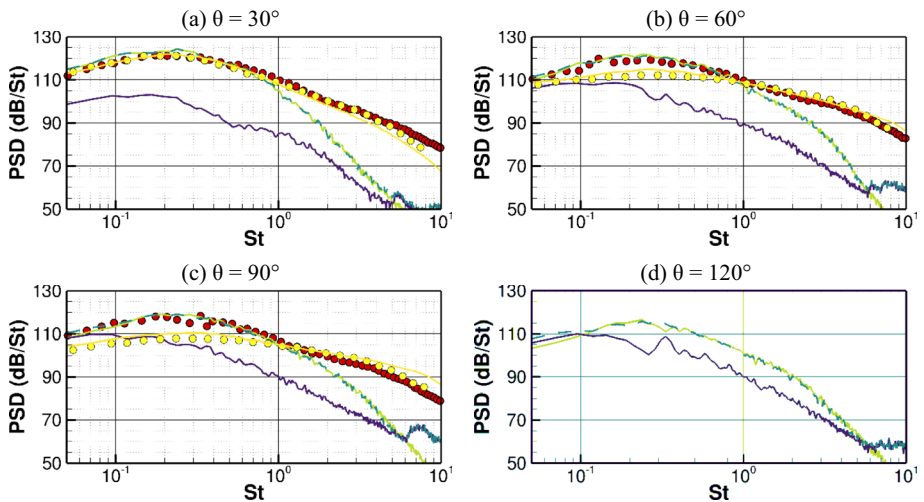


**Fig. 33** Pressure PSDs on the azimuthal antenna, shielded side ( $\Phi = 80^\circ$ ). Isolated jet: Yellow circle Exp. Pprime; yellow line simulation. Installed jet: red circle Exp. Pprime; light green line simulation, direct contribution ( $p_I'$ ); purple line simulation, reflected contribution ( $p_{II}'$ ); green line simulation, total contribution ( $p_I' + p_{II}'$ )

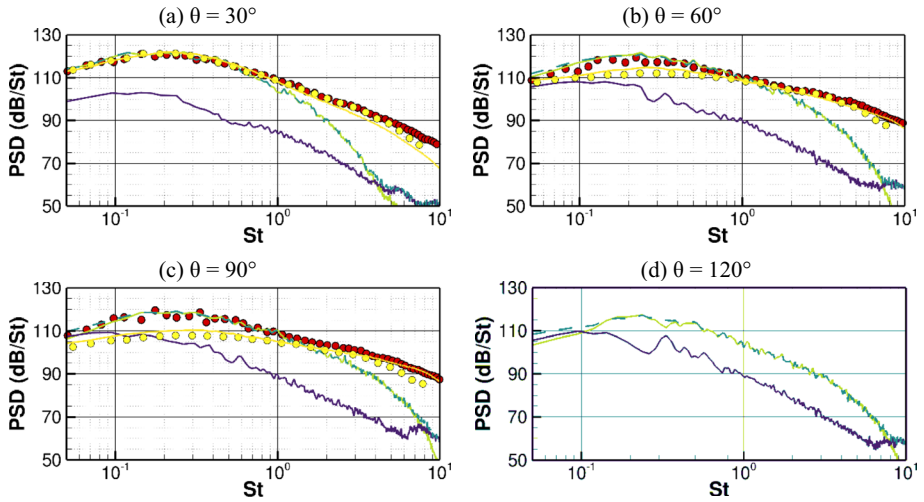


**Fig. 34** Pressure PSDs on the azimuthal antenna, unshielded side ( $\Phi=260^\circ$ ). Isolated jet: Yellow circle Exp. Pprime; yellow line simulation. Installed jet: red circle Exp. Pprime; light green line simulation, direct contribution ( $p_{I'}$ ); purple line simulation, reflected contribution ( $p_{II'}$ ); green line simulation, total contribution ( $p_{I'} + p_{II'}$ )

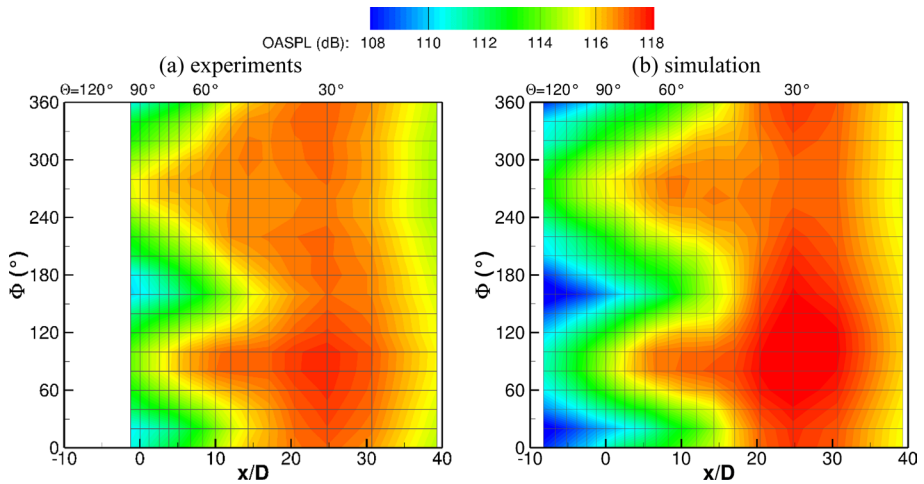


**Fig. 35** Experimental and simulated integrated pressure levels on the azimuthal antenna

to the direct contribution (it is recalled the high-frequency reflected levels are spurious noise and must not be considered). The predominance of the direct contribution is still observed farther upstream, for  $\theta = 120^\circ$ , even if the pressure levels of direct and reflected contribution are comparable below  $St = 0.1$ . Generally speaking, the role of the plate on the radiated noise is well captured numerically.

Pressure levels on the unshielded side ( $\Phi = 260^\circ$ ) are visible in Fig. 34. Previous conclusions drawn for the shielded side also apply here, with nevertheless a better agreement between the simulation and the experiments at low frequencies for  $\theta = 30^\circ$ .

Next, cartographies of the integrated pressure levels along the axial and azimuthal directions are reproduced in Fig. 35. We recall azimuthal angles  $0^\circ \leq \Phi \leq 180^\circ$  correspond to the shielded side ( $y \geq 0$ ) whereas  $180^\circ \leq \Phi \leq 360^\circ$  correspond to the unshielded side ( $y \leq 0$ ). First, the geometry being symmetric along the plane  $z=0$ , integrated levels are expected to be symmetric with respect to the azimuthal angle  $\Phi=90^\circ$  for the shielded side and  $\Phi=270^\circ$  for the unshielded side. This is indeed the case numerically, which confirms the correct statistical convergence of the levels as expected from isolated jet results, Sect. 4.7.2. The variations of the integrated levels are correctly captured numerically and the azimuthal variation of the pressure level caused by the plate is accurately reproduced. The highest levels are observed on the shielded side, levels are lower on the unshielded side and the minimum levels are found near the sideline direction ( $\Phi=20^\circ$  and  $160^\circ$ ) for  $x/D \leq 10$ . More quantitatively, the agreement lies below 0.3 dB for most of the observation angles, except in the downstream arc ( $x/D \geq 20$ ) and in particular on the shielded side where the simulation is up to 1 dB larger than the measurements.

The quantitative comparison between the experiments and the simulation is better visible in Fig. 36, with the axial evolution of the pressure levels above ( $\Phi=80^\circ$ ) and below ( $\Phi=260^\circ$ ) the plate. For  $x/D=25$  ( $\theta=30^\circ$ ), the level on the shielded side is 1 dB higher than on the unshielded side in the experiments and 1.5 dB in the simulation. In addition to the total radiated noise, the direct contribution is also reproduced in the figure. Direct and total contributions match downstream ( $x/D \geq 15$ ,  $\theta \leq 45^\circ$ ) but slightly differ for lower axial positions, which evidences the contribution of the reflections on the plate to the total noise. The reflected contribution is 7 to 10 dB lower than the direct contribution for these positions and is not reproduced in the figure, but it is sufficient to modulate the direct contribution up to 0.4 dB. It is worth noting the reflections on the plate improve the agreement between the experiments and the simulation by increasing noise for  $x/D \leq 0$  (constructive interferences between direct and reflected contributions), whereas noise is decreased for  $0 \leq x/D \leq 15$  (destructive interferences).

Figure 37 gives the separate contributions of direct and reflected contributions on the azimuthal antenna. Overall, direct contribution is always higher than reflected one. The highest reflected levels are found for  $x/D \leq 10$  ( $\theta \geq 55^\circ$ ) on the lateral azimuthal direction,  $\Phi \sim 0^\circ$  and  $180^\circ$ , where their contribution on the total levels are expected to be the largest.

This expectation is confirmed with the azimuthal profiles of the integrated levels, visible in Fig. 38. Reflected noise has no contribution downstream ( $\theta=30^\circ$ ) and starts to be visible for  $\theta=60^\circ$ . For  $\theta=90^\circ$  and  $120^\circ$  reflections contribute to the total for all azimuthal angles. Their highest contribution is found near  $\Phi \sim 0^\circ$  and  $180^\circ$  where the

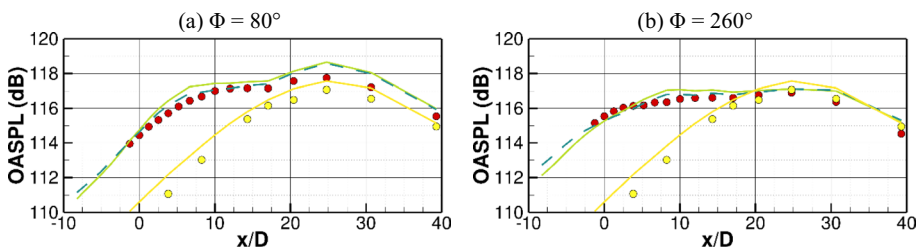


**Fig. 36** Axial evolution of the integral pressure levels on the shielded ( $\Phi=80^\circ$ ) and unshielded sides ( $\Phi=260^\circ$ ) of the azimuthal antenna. Isolated jet: yellow circle Exp. Pprime; yellow line simulation. Installed jet: red circle Exp. Pprime; light green line simulation, direct contribution ( $p_l'$ ); green line simulation, total contribution ( $p_l' + p_{ll}'$ )

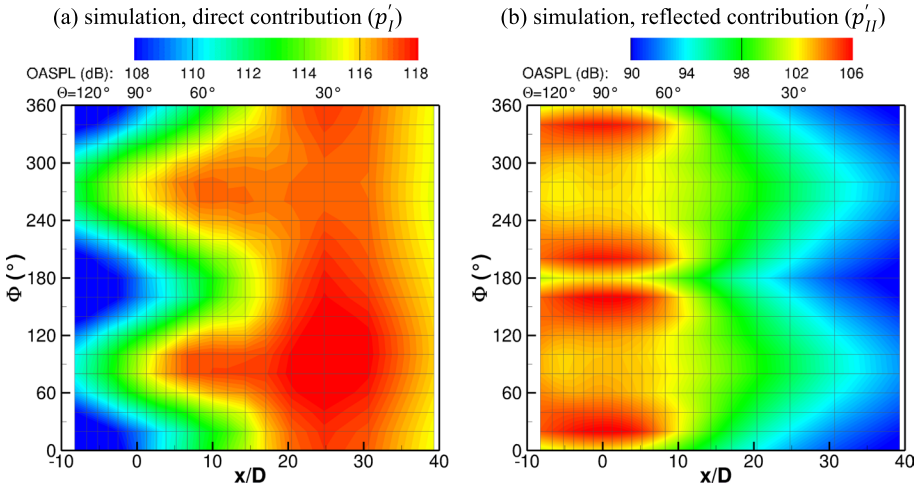


Fig. 37 Direct ( $p_I'$ ) and reflected ( $p_{II}'$ ) contribution of the simulated noise on the azimuthal antenna

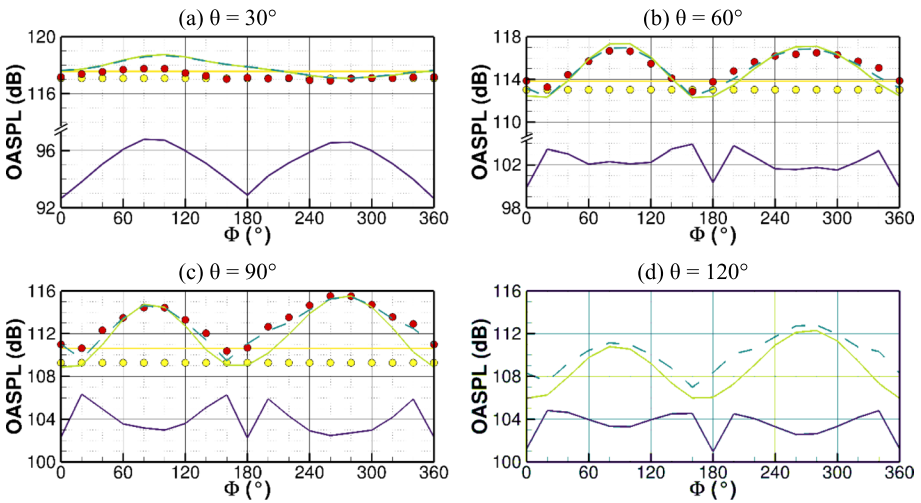


Fig. 38 Azimuthal evolution of the integral pressure levels for different axial positions of the azimuthal antenna. Isolated jet: yellow circle Exp. Pprime; yellow line simulation. Installed jet: red circle Exp. Pprime; light green line simulation, direct contribution ( $p_I'$ ); purple line simulation, reflected contribution ( $p_{II}'$ ); green line simulation, total contribution ( $p_I' + p_{II}'$ )

direct contribution is also the lowest, leading to differences between the direct contribution and total level of several dB. This, again, illustrates the role of the reflections on the flat plate to accurately reproduce the experimental levels.

## 6 Conclusions

This article focuses on the numerical simulation of jet noise installation effects through the coupling of an advanced Computational Fluid Dynamics (CFD) method for prediction of the noise sources and an integral formulation to reconstruct the time pressure histories at microphones positions. The case considered is an isothermal single stream nozzle at Mach number 0.9 and with diameter-based Reynolds number of  $10^6$ . The turbulent boundary layer inside the nozzle is reproduced through the use of Zonal Detached Eddy Simulation, which acts as a Wall Modelled Large-Eddy-Simulation in attached boundary layers (ZDES mode 3), together with the inclusion of roughness elements in the computational domain using Immersed Boundary Conditions to generate turbulence. The numerical grid is unstructured, mainly composed of tetrahedra, to cluster the grid points in the jet shear layer and to get rid of the limitations imposed by structured grid approach.

The numerical approach is first validated for the isolated configuration. The grid convergence is investigated for 3 meshes varying from  $73.8 \times 10^6$  to  $181.5 \times 10^6$  elements. It is concluded that a coherent grid densification must be achieved between the source generation and noise propagation areas to be best efficient. Additionally, statistical data are found to be converged for  $600 D/U_j$  long time signals, this duration being possibly reduced to  $300 D/U_j$  when the data are azimuthally averaged. For the highest grid density, simulated noise levels are globally accurately simulated at least up to  $St = 8$ , the highest experimental frequency available, and integrated pressure levels collapse within 1 dB with the experiments. The installed configuration is investigated in a second time and builds on the previous conclusions. A noise radiation methodology based on integral methods is proposed to reconstruct the pressure signals at microphone locations with a reduced numerical cost. Noise generation and propagation in the CFD simulation is limited to the jet plume and jet-plate interaction areas, whereas sound reflections on the plate are modelled during a two-step radiation process. The simulation compares very favorably with the experimental data, azimuthal noise variations induced by the plate are correctly captured and noise levels collapse within 1 dB.

The results presented in this article give confidence in the numerical capability to accurately predict installed jet noise. The simulation process seems mature enough to be used both for industrial assessment of new design and in prospective research studies in conjunction with experiments, for instance to derive JSI noise mitigation strategies. A potential bottleneck for the application of the noise radiation method is the important surface storage, required to reach statistical convergence, and all the more important as the target cut-off frequency is large and requires a dense grid. This limitation could be alleviated through the use of an acoustic co-processing where far-field pressure reconstruction is performed on the fly, along with the CFD simulation.

## Appendix 1 Detailed computational methodologies

### 1.A Zonal Detached Eddy Simulation

The ZDES is based on the basic idea of the original Detached Eddy Simulation (Spalart et al. 1997) (DES97) which relies on the Spalart–Allmaras (SA) RANS model (Spalart and Allmaras 1994). A brief description of the SA model is provided below, the reader is



referred to the original paper (Spalart and Allmaras 1994) for a full description. The SA model is based on the transport equation of a pseudo viscosity  $\tilde{\nu}$  involving production, diffusion and destruction terms:

$$\frac{D\tilde{\nu}}{Dt} = \underbrace{c_{b1}\tilde{S}\tilde{\nu}}_{production} + \underbrace{\frac{1}{\sigma}[\nabla \cdot ((\nu + \tilde{\nu})\nabla\tilde{\nu}) + c_{b2}(\nabla\tilde{\nu})^2]}_{diffusion} - \underbrace{c_{w1}f_w\left[\frac{\tilde{\nu}}{d_w}\right]^2}_{destruction} \tag{1}$$

where  $\nu$  is the dynamic viscosity,  $\sigma=2/3$ ,  $d_w$  is the distance to the wall,  $c_{b1}$ ,  $c_{b2}$  and  $c_{w1}$  are constants,  $\tilde{S}$  is a modified vorticity magnitude involving a near wall function  $f_{v2}$  and  $f_w$  is another near-wall function. The eddy viscosity entering the Boussinesq closure for the RANS equations is defined using a third near-wall function  $f_{v1} \cdot \nu_t = f_{v1}\tilde{\nu}$ . The three near-wall corrections  $f_w$ ,  $f_{v1}$  and  $f_{v2}$  were calibrated to ensure the correct behavior of  $\tilde{\nu}$  in the viscous, buffer, log-layer and outer parts of the boundary layer. The basic principle of DES97 is to modify the destruction term of eq. (1) so that the RANS eddy-viscosity is reduced to a LES subgrid scale one in detached areas. To do so, the distance to the wall in eq. (1) is replaced by  $\tilde{d}_{DES97} = \min(d_w, C_{DES}\Delta)$  with  $C_{DES}=0.65$  and  $\Delta = \Delta_{max}$  is the maximum cell size. With this modification, away from the walls, when production and destruction terms are balanced, the eddy viscosity scales with the local mesh size and the local vorticity modulus:  $\nu_t \approx S\Delta^2$  which is similar to Smagorinsky’s subgrid scale model.

Therefore the transport equation for ZDES reads:

$$\frac{D\tilde{\nu}}{Dt} = \underbrace{c_{b1}\tilde{S}\tilde{\nu}}_{production} + \underbrace{\frac{1}{\sigma}[\nabla \cdot ((\nu + \tilde{\nu})\nabla\tilde{\nu}) + c_{b2}(\nabla\tilde{\nu})^2]}_{diffusion} - \underbrace{c_{w1}f_w\left[\frac{\tilde{\nu}}{\tilde{d}_{ZDES}}\right]^2}_{destruction} \tag{2}$$

The hybrid length scale  $\tilde{d}_{ZDES}$  is defined for each mode 1, 2 and 3, see (Deck 2012). The present work focuses on the use of ZDES mode 3 which formulation is detailed in the following.

The mode 3 of ZDES was defined to act as a Wall Modelled LES in attached boundary layers. Let us be reminded that within WMLES, turbulence in the outer-layer is LES-resolved whereas a near-wall RANS zone plays the role of wall model. Therefore the definition of the hybrid length scale  $\tilde{d}_{ZDES}^{III}$  relies on the specification of a RANS/LES interface height  $d_w^{interface}$  within the boundary layer according to eq. (3):

$$\tilde{d}_{ZDES}^{III} = \begin{cases} d_w & \text{if } d_w < d_w^{interface}(x) \\ \min\left( \underbrace{d_w}_{\tilde{d}_{RANS}}, \underbrace{C_{DES}\Delta_{ZDES}^{III}}_{\tilde{d}_{LES}} \right) & \text{otherwise} \end{cases} \tag{3}$$

with  $\Delta_{ZDES}^{III} = \Delta_{vol} = vol^{(1/3)}$  where  $vol$  corresponds to the volume of the cell. In the present study, the value  $d_w^{interface}(x) = 0.1\delta(x)$  was chosen.  $\delta(x)$  is the local boundary layer thickness and is determined by a precursor RANS calculation. See (Deck et al. 2014; Renard and Deck 2015) for further discussion of the interface location. ZDES mode 3 was used and validated for WMLES in (Stich et al. 2019; Deck and Laraufie 2013; Renard and Deck 2015; Laraufie and Deck 2013).

## 1.B Turbulence Generation Using Immersed Boundary Condition

Instead of using a body-fitted grid to account for wall boundaries, the basic idea of the IBC method is to mark the solid and fluid zones of the computational mesh and to take into account the wall presence by adding a source term in the Navier Stokes equations in order to mimic a solid boundary.

The formulation of the IBC method used in this study is identical to the one detailed in (Deck et al. 2018), which was first proposed in (Mochel et al. 2014) and was inspired by the direct forcing approach of (Mittal and Iaccarino 2005; Fadlun et al. 2000) adapted to curvilinear grids and RANS/LES methods. The source term entering the Navier–Stokes equations for the IBC forcing is defined so that the momentum and pseudo eddy viscosity quantities return to zero, thus acting as a solid boundary. The roughness elements are introduced in order to produce streamwise vorticity in the boundary layer at the location where it is most likely to be amplified and thus generate resolved turbulence to initiate the WMLES behavior of ZDES mode 3. The most suited shape parameters of the roughness elements were identified in (Deck et al. 2018) using a parametric study. Note that in (Deck et al. 2018), the authors also used the Dynamic Forcing method (DF; Laraufie et al. 2011) to accelerate the development of three-dimensional turbulence downstream of the roughness elements. This method was not used in the present work since the length of the nozzle duct is large enough for the turbulence generated by the tripping dots to develop at an affordable CPU cost without the need of DF (see Sect. 4.2).

## 1.C Noise Radiation

For the isolated jet configuration, the pressure  $p_l'$  radiated at the observer location  $\vec{x}$  can be calculated in the time domain using one of the two following formulas developed at ONERA from the FWH surface formulation (Prieur and Rahier 2001; Rahier et al. 2015).

$$p_l'(\vec{x}, t) = \int_{\tau} \int_S \left( F_{FWH} + \frac{\partial F'_{FWH}}{\partial \tau} \right) G dS d\tau \tag{4}$$

$$p_l'(\vec{x}, t) = \int_{\tau} \int_S F_{FWH}(\vec{x}, \vec{y}, \tau) G dS d\tau + \frac{\partial}{\partial t} \int_{\tau} \int_S F'_{FWH}(\vec{x}, \vec{y}, \tau) G dS d\tau \tag{5}$$

where  $F_{FWH} = \frac{\beta^2}{d^2} \Sigma_1$ ,  $F'_{FWH} = \frac{\Sigma_1}{a_0 d} + \frac{\Sigma_2}{\beta^2}$ ,  $\Sigma_1 = \left( A_i(x_i - y_i) + \frac{(M_0^2 A_i - U_0 B)}{\beta^2} (x_i - y_i) \right)$ ,  $\Sigma_2 = B - \frac{M_0 A_i}{a_0}$ ,  $G = \frac{\delta(g)}{4\pi d}$ ,  $A_i = p' n_i + \rho(u_i - U_0 \delta_{1i})(u_n - v_n)$ ,  $B = \rho_0(v_n - U_0 n_1) + \rho(u_n - v_n)$ ,  $u_n = \vec{u} \cdot \vec{n}$ ,  $v_n = \vec{v} \cdot \vec{n}$ ,  $g = \tau - t + \sigma/a_0$ ,  $\sigma = (d - M_0(x_1 - y_1))/\beta^2$ ,  $d = \sqrt{C_i(x_i - y_i)^2}$ ,  $C_i = (1 - \beta^2)\delta_{1i} + \beta^2$ ,  $\beta^2 = 1 - M_0^2$ ,  $M_0 = U_0/a_0$  with  $a_0$  the speed of sound in the unperturbed medium,  $U_0$  the velocity of the uniform flow aligned with  $x_1$  axis,  $p'$  the pressure fluctuation,  $\rho$  the density,  $\rho_0$  the density of the unperturbed fluid,  $\vec{u}$  and  $\vec{v}$  respectively the fluid velocity and the control surface velocity,  $\vec{n}$  the unit normal vector on the control surface,  $x_i$  the observer space coordinates,  $y_i$  the control surface space coordinates,  $\tau$  and  $t$  respectively the emission and the reception times (more details in (Prieur and Rahier 2001; Delrieux 2003).

Formula (4), (Prieur and Rahier 2001) is limited to fixed integration surfaces but has the advantage of providing more regular signals than formula (5). On the one hand, the

time derivative outside the integration in formula (5), (Delrieux 2003) tends to amplify the numerical noise of the acoustic calculation at its frequency sampling and a few sub-harmonics. On the other hand, it significantly simplifies the expression of additional terms (not present in formula (5)) that have been developed for integration surfaces crossed by turbulent flows (Rahier et al. 2015). These additional terms allow the use of such surfaces while avoiding spurious noise generated by turbulence (Rahier et al. 2004). For jet noise computations, the use of closed integration surfaces (as the FWH formulation theoretically requires), together with these additional surface terms, improve in particular the acoustic predictions in the low-frequency part of the spectra (Rahier et al. 2015). Therefore, the acoustic calculations presented in this study are carried out using expression (5) supplemented by these additional terms.

For the installed jet configuration, the complementary acoustic calculation  $p_{II}'$  is performed using the following classic Kirchhoff formula for a fixed integration surface  $S_K$  (Prieur and Rahier 2001):

$$p'_{II}(\vec{x}, t) = \int_{\tau} \int_{S_K} F_K(\vec{x}, \vec{y}, \tau) G dS d\tau \tag{6}$$

where  $F_K = \beta^2 \frac{(x_i - y_i)n_i}{d^2} p'_{ref} - \frac{\partial p'_{ref}}{\partial y_i} n_i + M_0^2 n_1 \frac{\partial p'_{ref}}{\partial y_1} + \frac{1}{a_0} \left( \frac{(x_i - y_i)n_i}{d} + M_0 n_1 \right) \frac{\partial p'_{ref}}{\partial \tau}$ .

In the expression of  $F_K$ ,  $p'_{ref}$  is the reflected pressure on the plate surface. This reflected pressure, its gradient  $\partial p'_{ref} / \partial y_i$  and its time derivative  $\partial p'_{ref} / \partial t$  are simply determined as a function of the incident pressure  $p'_{inc}$ , its gradient  $\partial p'_{inc} / \partial y_i$  (numerically calculated by finite differences on a double layer on either side of the plate skin) and its time derivative  $\partial p'_{inc} / \partial t$  (these quantities being provided by the first calculation), the local normal to the surface  $\vec{n}_K$ , and the observer location  $\vec{x}$ . The model is based on the assumptions of rigid wall and locally planar reflections that lead to following relationships between incident pressure and reflected pressure:

Observer on reflection side:  $p'_{ref} = p'_{inc}$ ,  $\frac{\partial p'_{ref}}{\partial \tau} = \frac{\partial p'_{inc}}{\partial \tau}$ ,  $\frac{\partial p'_{ref}}{\partial y_i} = \frac{\partial p'_{inc}}{\partial y_i} - 2 \frac{\partial p'_{inc}}{\partial y_k} n_k n_i$ .

Observer on shadow side:  $p'_{ref} = -p'_{inc}$ ,  $\frac{\partial p'_{ref}}{\partial \tau} = -\frac{\partial p'_{inc}}{\partial \tau}$ ,  $\frac{\partial p'_{ref}}{\partial y_i} = -\frac{\partial p'_{inc}}{\partial y_i}$ .

The reflection and shadow sides are determined for each cell of  $S_K$  at each time step from the values of  $\partial p'_{inc} / \partial y_i$ ,  $\partial p'_{inc} / \partial t$ ,  $\vec{n}_K$  and  $\vec{x}$ . The resulting pressure  $p'_{II}(\vec{x}, t)$  is added to the free-field radiation  $p'_I(\vec{x}, t)$ .

Despite this hypothesis of locally planar reflections, the method can nevertheless predict fairly realistic reflection and shadow effects for curved surfaces (see an example of qualitative comparison in Fig. 39). On the other hand, because of this hypothesis of small

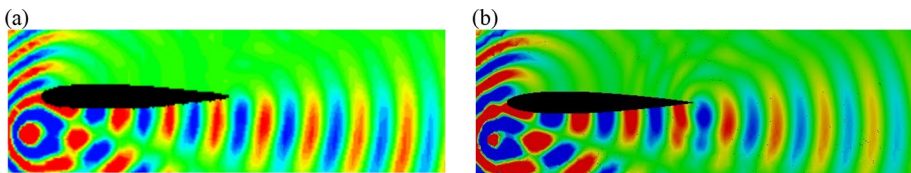


**Fig. 39** Instantaneous acoustic pressure scattered by a NACA 0012 profile. 2D configuration, uniform flow at Mach number 0.5, point harmonic source in the vicinity of the leading edge. **a** Kirchhoff method applied to the profile skin, **b** Euler acoustic calculation

wavelength with respect to the reflecting surface local curvature, this approach only partially predicts diffraction effects. This is why in the present study the trailing edge of the plate is enclosed as much as possible in FWH porous surface (see Sect. 5.2.1). This approach assumes a uniform mean flow and thus does not account for refraction effects.

For both formulations, the time derivatives are calculated by second-order centered finite differences. The computations are carried out starting from the emission times  $\tau_j$  and the pressures at the prescribed reception times  $t_k$  are calculated by linear interpolations of the pressures obtained at the reception times  $t_j = \tau_j + \sigma/a_0$  and  $t_{j+1} = \tau_{j+1} + \sigma/a_0$  on either side of time  $t_k$ . The time integration scheme is thus also of second order.

## Appendix 2 Azimuthal Correlation of Radiated Noise

The correlation coefficients along the azimuthal direction of the time histories of pressure radiated on the azimuthal array are computed in this appendix for the isolated jet. For two time signals  $s_1(t)$  and  $s_2(t)$ , the correlation coefficient  $c_{s_1,s_2}$  writes

$$c_{s_1,s_2} = \frac{\sigma_{s_1,s_2}}{\sigma_{s_1} \sigma_{s_2}}$$

with  $\sigma_{s_1,s_2}$  the covariance

$$\sigma_{s_1,s_2} = \overline{(s_1(t) - \overline{s_1(t)})(s_2(t) - \overline{s_2(t)})}$$

$\sigma_s$  the standard deviation

$$\sigma_s = \sqrt{\overline{\sigma_{s,s}}}$$

and where  $(\cdot)$  corresponds to time averaging. To investigate the variation of the correlation with the frequency bandwidth, a low-pass, bass-band or high-pass filter is first applied to the time signals prior to computing the correlation coefficients. This filtering is performed in the frequency domain (non-causal filtering). First, the Fast Fourier Transform (FFT) of the time signals are computed; second, all coefficients outside the bandwidth of interest are nullified; third, time signals are reconstructed using an Inverse FFT (IFFT). The four filters considered are summarized in Table 2.

The analysis is performed with  $2100 D/U_j$  long time signals and the correlation coefficient is computed for each axial position of the azimuthal antenna. The azimuthal evolution of the correlation coefficient is reproduced in Fig. 40 for four axial positions and the four frequency filtering mentioned above.

For the full signal, the azimuthal correlation is very large for the low observation angles and reduces as the observation angle grows. At  $20^\circ$ , the minimum correlation coefficient

**Table 2** Frequency bandwidths considered for the frequency filtering of the pressure signal

	Stmin	Stmax
Full signal	–	–
Low-pass filter signal	0.05	0.1
Band-pass filter signal	0.1	1.0
High-pass filter signal	1.0	10.0

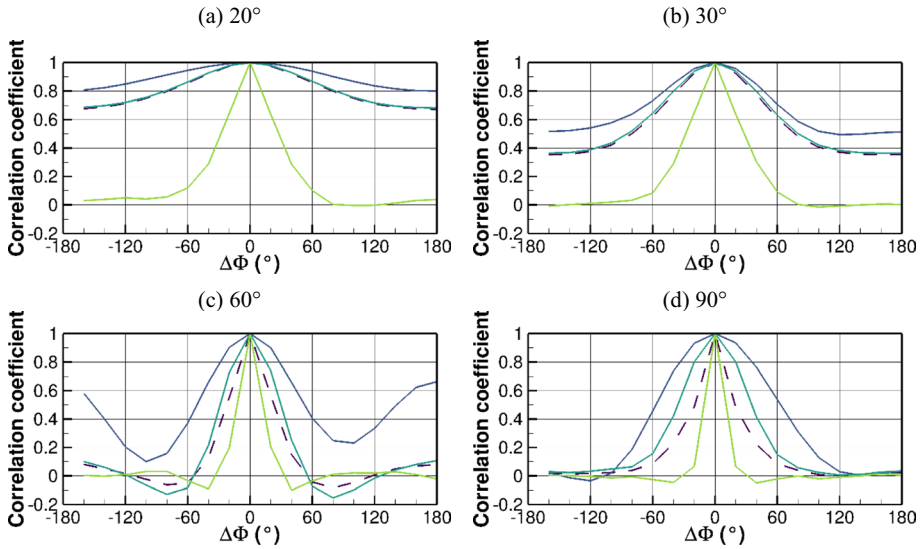


**Fig. 40** Azimuthal evolution of the correlation coefficient for the radiated pressure purple dashed line full signals; blue line low-pass filter signals; green line band-pass filter signals; light green line high-pass filter signals

is 0.7 for the maximum angular distance  $\Delta\Phi=180^\circ$ . A correlation of 0.6 is observed for  $\Delta\Phi=60^\circ$  at  $30^\circ$ , whereas the angular distance drops below  $\Delta\Phi=20^\circ$  at  $60^\circ$  and  $90^\circ$  for the same correlation level. For these two latter observation angles of  $60^\circ$  and  $90^\circ$ , the correlation rapidly falls to zero for larger angular distances.

Considering the filtered signals, the evolution of the correlation coefficient is qualitatively similar for the four observation angles reproduced. The largest correlations are observed for the low-pass filtered signals, and the correlation levels decay as the frequency bandwidth considered grows. Generally speaking, correlations levels are always higher for low observation angles ( $20^\circ$  and  $30^\circ$ ) and decrease as the observation angle rises ( $60^\circ$  and  $90^\circ$ ).

### Appendix 3 Assessment of the noise radiation methodology for the installed jet.

The accuracy of the noise radiated with the two-step acoustic methodology for the installed configuration is evaluated with a sensitivity study similar to that of the isolated jet, for sensors on the azimuthal antenna as well as near-field sensors illustrated in Fig. 41. In the presence of the plate, the surface S0 is too close from the jet and underestimates the levels for  $St < 0.3$  for locations upstream of the trailing edge. This underestimation reduces as the surface is farther away from the jet and levels are globally converged for surface S2. It is assumed surface S0 is too tight to include all the additional noise sources associated with turbulence scattering at the trailing edge. In the downstream end, pressure levels are found to be independent of the axial extent of the surface and the surface S2-D1-D2 is used for

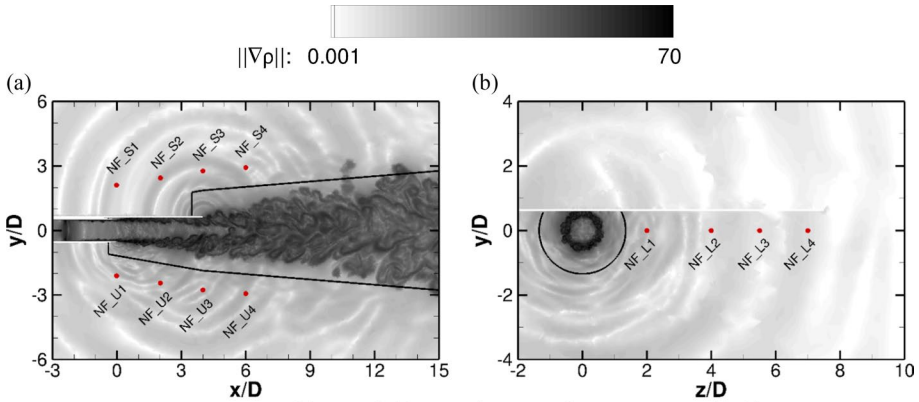


**Fig. 41** Position of the near-field sensors (porous surface S2-D1-D2 is in black). **a** plane  $z=0$ , **b** plane  $x/D=1$

all the analyses below. From the isolated jet results, noise is expected to be accurate up to  $St=1$ .

In addition, the sensitivity of the radiated noise to the discretization of the plate has been verified numerically. It corresponds to the surface discretization of the plate, which needs to be sufficiently fine to capture high-frequency fluctuations, and the numerical evaluation of the incident pressure gradient on the plate (see Appendix 1.C), which is evaluated by finite differences on a double layer on either side of the plate skin, for both shielded and unshielded sides. Results are found to be independent of the plate discretization for the frequencies of interest when the surface is discretized with at least 5 points per wavelength  $\lambda_{min}$  at the highest resolved frequency ( $St_{max}=1$ ) and with a double layer thickness of  $\lambda_{min}/50$  to  $\lambda_{min}/100$ . In the following, a plate discretization of  $\lambda_{min}/10$  and double layer thickness of  $\lambda_{min}/100$  are used for all simulations.

The validation of the radiation methodology is achieved by comparing the pressure radiated on the near-field sensors of Fig. 41 with the pressure data directly extracted from the CFD simulation, and which include all the sound production and propagation effects from the mean flow and the solid surfaces. This analysis also makes possible quantifying the contribution of acoustic reflections on the plate to the total pressure. Indeed, the radiation methodology separates the direct radiation from the porous surface to the sensors, labelled as *direct contribution* hereafter, to that of the acoustic reflections on the solid surface, labelled as *reflected contribution*. When the porous surface is designed to include only the noise sources (from the turbulent jet and turbulence scattering by the trailing edge) and not the acoustic reflections on the solid surfaces outside the jet, as done here, both contributions are distinct.

The simulated and radiated (total contribution) pressure spectra on the shielded (above the plate) sensors are illustrated in Fig. 42. Globally, both spectra collapse for low frequencies, which validates the radiation methodology. One may however notice a slight underestimation of the radiated levels for the low frequencies for the most upstream sensors, which vanishes for  $x/D \geq 2$ . The spectra agree up to  $St \sim 0.8$ , above which CFD levels fall rapidly because of the numerical dissipation. It is worth noting the plateau visible for the radiated

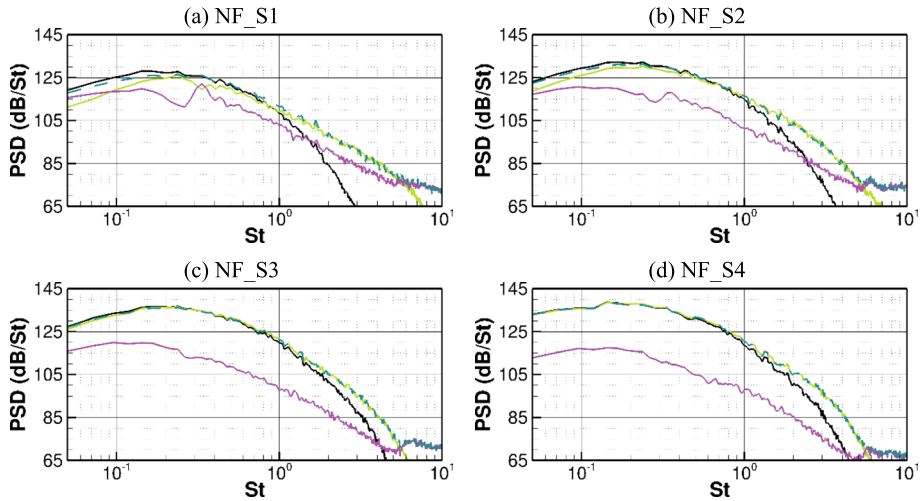


**Fig. 42** Pressure PSDs on the shielded near-field sensors. Black line CFD; light green line radiated, direct contribution ( $p_I'$ ); light purple line radiated, reflected contribution ( $p_{II}'$ ); green line radiated, total contribution ( $p_I' + p_{II}'$ )

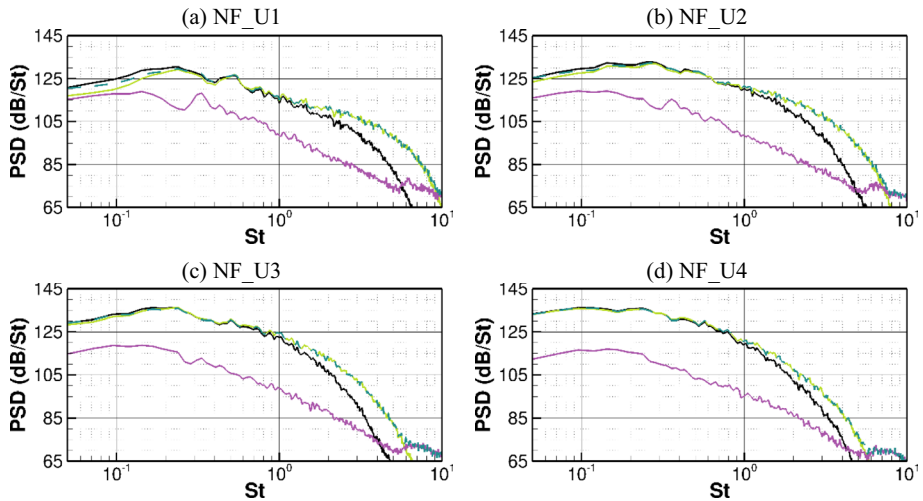


**Fig. 43** Pressure PSDs on the unshielded near-field sensors. Black line CFD; light green line radiated, direct contribution ( $p_I'$ ); light purple line radiated, reflected contribution ( $p_{II}'$ ); green line radiated, total contribution ( $p_I' + p_{II}'$ )

pressure above  $St \sim 5$  must be disregarded as it is a numerical artefact caused by the insufficient discretization of the surface for such frequencies.

For sensors NF\_S3 and NF\_S4, located downstream of the trailing edge, reflections on the flat plate do not significantly contribute to the total pressure levels. Reflections get all the more important as the sensor is moved far upstream of the trailing edge. They essentially occur for low frequencies and need to be accounted for to recover the CFD levels, as

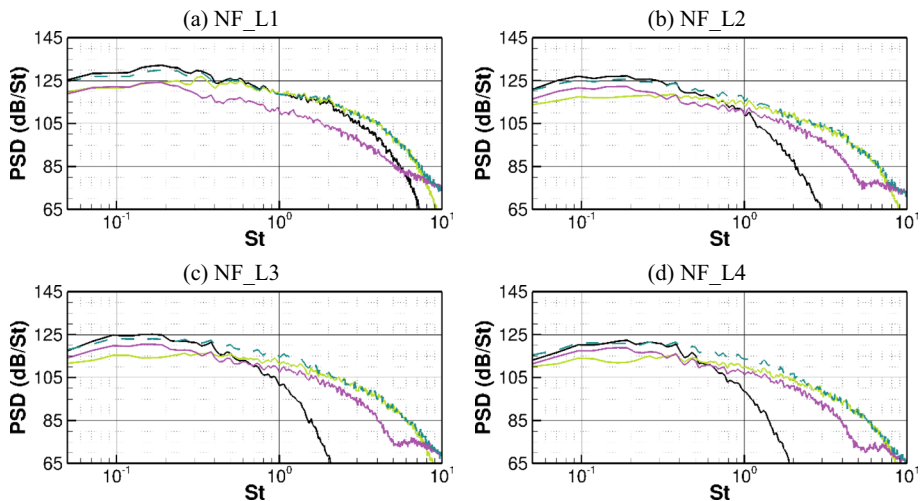


**Fig. 44** Pressure PSDs on the lateral near-field sensors. Black line CFD; light green line radiated, direct contribution ( $p_I'$ ); light purple line radiated, reflected contribution ( $p_{II}'$ ); green line radiated, total contribution ( $p_I' + p_{II}'$ )

they exhibit levels similar to those of the direct radiation. For sensors NF\_S2, direct contribution for instance underestimates the CFD levels by 4 dB, and this underestimation rises to 8 dB for sensor NF\_S1.

The previous observations for the shielded sensors also apply for the unshielded sensors visible in Fig. 43. One may simply note that contributions of the reflections for the upstream sensors are lower on the unshielded side compared to the shielded side.

To end the validation, pressure spectra are reproduced in Fig. 44 for lateral sensors below the plate, one diameter downstream of the nozzle exit. Again, the radiated spectra collapse with the CFD data in the low frequency range. There is no specific grid refinement to capture the acoustic waves as they propagate away from the jet axis in CFD, so that numerical dissipation is large and pressure levels rapidly drop for medium and high frequencies, whereas those levels are better captured with the integral method. For these sensors, contributions of reflections are as large as or larger than the direct contribution at low frequencies, and only a few dB below the direct contribution in the medium frequency range, which highlights the role of acoustic reflections on the surface for the pressure levels in this area.

**Acknowledgements** The authors are grateful to Dr Peter Jordan and Dr Matteo Mancinelli from Pprime for sharing the experimental data of the installed jet.

**Author contributions** FG: performed the aerodynamic simulations, GR: developed the numerical methodology to account for reflection surface in noise radiation, GR and MH: derived the noise radiation methodology for the installed jet, MH: performed the noise radiation simulations, FG and MH: analyzed the aerodynamic and acoustic results. The first draft of the manuscript was written by MH, with contributions from FG and GR. All authors revised the manuscript, read and approved the final version.

**Funding** This work has been performed in the frame of the EU DJINN (Decrease Jet Installation Noise) project. DJINN project receives funding from the European Union's Horizon 2020 research and innovation programme under grant agreement No 861438. DJINN is a collaborative effort between CFD-Berlin (coordinator), Airbus SAS, Dassault Aviation, Safran Aircraft Engines, Rolls-Royce Deutschland, ONERA,



DLR, University of Southampton, CERFACS, Imperial College London, von Karman Institute, CNRS, and Queen Mary University of London. This work was granted access to the HPC resources of CINES under the allocation 2021-A0102A12442 made by GENCI.

## Declarations

**Conflict of interest** The authors declare that they have no conflict of interest.

**Open Access** This article is licensed under a Creative Commons Attribution 4.0 International License, which permits use, sharing, adaptation, distribution and reproduction in any medium or format, as long as you give appropriate credit to the original author(s) and the source, provide a link to the Creative Commons licence, and indicate if changes were made. The images or other third party material in this article are included in the article's Creative Commons licence, unless indicated otherwise in a credit line to the material. If material is not included in the article's Creative Commons licence and your intended use is not permitted by statutory regulation or exceeds the permitted use, you will need to obtain permission directly from the copyright holder. To view a copy of this licence, visit <http://creativecommons.org/licenses/by/4.0/>.

## References

- Andersson, N., Eriksson, L.-E., Davidson, L.: Large-Eddy Simulation of subsonic turbulent jets and their radiated. *AIAA J.* **43**, 1899–1912 (2005)
- Angelino, M., Xia, H., Page, G.J.: Adaptive Wall-Modelled Large Eddy Simulation of jet noise in isolated and installed configurations. in Proceedings of the 24th AIAA/CEAS Aeroacoustics Conference, Paper AIAA 2018–3618 (2018)
- Angelino, M., Moratilla-Vega, M.A., Howlett, A., Xia, H., Page, G.J.: Numerical investigation of installed jet noise sensitivity to lift and wing/engine positioning. in Proceedings of the 25th AIAA/CEAS Aeroacoustics Conference, Paper AIAA 2019–2770, (2019)
- Bailly, C., Fujii, K.: High-speed jet noise. *Mech. Eng. Rev.* **3**(1), 15–00496 (2016)
- Bailly, C., Bogey, C., Marsden, O.: Progress in direct noise computation. *Int. J. Aeroacoustics* **9**, 123–143 (2010)
- Belyaev, I.V., Zaytsev, M.Y., Kopiev, V.F., Ostrikov, N.N., Faranosov, G.A.: Studying the effect of flap angle on the noise of interaction of a high-bypass jet with a swept wing in a co-flow. *Acoust. Phys.* **63**, 14–25 (2017)
- Bodony, D.J., Lele, S.K.: On using Large-Eddy Simulation for the prediction of noise from cold and heated turbulent jets. *Phys. Fluids* (2005). <https://doi.org/10.1063/1.2001689>
- Bogey, C., Bailly, C.: Effects of inflow conditions and forcing on subsonic jet flows and noise. *AIAA J.* **43**, 1000–1007 (2005). <https://doi.org/10.2514/1.7465>
- Bogey, C., Marsden, O.: Simulations of initially highly disturbed jets with experiment-like exit boundary layers. *AIAA J.* **54**(4), 1299–1312 (2016). <https://doi.org/10.2514/1.J054426>
- Bogey, C., Sabatini, R.: Effects of nozzle-exit boundary-layer profile on the initial shear-layer instability, flow field and noise of subsonic jets. *J. Fluid Mech.* **876**, 288–325 (2019). <https://doi.org/10.1017/jfm.2019.546>
- Bogey, C., Barré, S., Bailly, C.: Direct computation of the noise generated by subsonic jets originating from a straight pipe nozzle. *Int. J. Aeroacoustics* **7**, 1–22 (2008)
- Bogey, C., Barré, S., Juvé, D., Bailly, C.: Simulation of a hot coaxial jet: direct noise prediction and flow-acoustics correlations. *Phys. Fluids* (2009). <https://doi.org/10.1063/1.3081561>
- Bogey, C., Marsden, O., Bailly, C.: Influence of initial turbulence level on the flow and sound fields of a subsonic jet at a diameter-based Reynolds number of  $10^5$ . *J. Fluid Mech.* **701**, 352–385 (2012)
- Bogey, C., Marsden, O., Bailly, C.: Large-Eddy Simulation of the flow and acoustic fields of a Reynolds number  $10^5$  subsonic jet with tripped exit boundary layers. *Physics of Fluids* **23** (2011)
- Bondarenko, M., Hu, Z., Zhang, X.: Large-Eddy Simulation of the interaction of a jet with a wing. in Proceedings of the 18th AIAA/CEAS Aeroacoustics Conference, Paper AIAA 2012–2254 (2012)
- Brès, G.A., Jordan, P., Jaunet, V., Le Rallic, M., Cavalieri, A.V.G., Towne, A., Lele, S.K., Colonius, T., Schmidt, O.T.: Importance of the nozzle-exit boundary-layer state in subsonic turbulent jets. *J. Fluid Mech.* **851**, 83–124 (2018). <https://doi.org/10.1017/jfm.2018.476>
- Bühler, S., Kleiser, L., Bogey, C.: Simulation of subsonic turbulent nozzle jet flow and its near-field sound. *AIAA J.* **52**(8), 1653–1669 (2014). <https://doi.org/10.2514/1.J052673>

- Bychkov, O.P., Faranosov, G.A.: An experimental study and theoretical simulation of jet-wing interaction noise. *Acoust. Phys.* **64**, 437–452 (2018)
- Cambier, L., Heib, S., Plot, S.: The Onera elsA CFD software: input from research and feedback from industry. *Mech. Industry* **14**, 159–174 (2013). <https://doi.org/10.1051/meca/2013056>
- Cavallieri, A.V.G., Jordan, P., Wolf, W.R., Gervais, Y.: Scattering of wave packets by a flat plate in the vicinity of a turbulent jet. *J. Sound Vib.* **333**, 6516–6531 (2014)
- Davy, R., Mortain, F., Huet, M., Le Garrec, T.: Installed jet noise source analysis by microphone array processing. in Proceedings of the 25th AIAA/CEAS Aeroacoustics Conference, Paper AIAA 2019–2654, (2019)
- da Silva, F.D., Deschamps, C.J., d. Silva, A.R., Simões, L.G.: Assessment of jet-plate interaction noise using the Lattice Boltzmann Method. in Proceedings of the 21st AIAA/CEAS Aeroacoustics Conference, Paper AIAA 2015–2207 (2015)
- Deck, S.: Recent improvements of the Zonal Detached Eddy Simulation (ZDES) formulation. *Theoret. Comput. Fluid Dyn.* **26**, 523–550 (2012). <https://doi.org/10.1007/s00162-011-0240-z>
- Deck, S., Laraufige, R.: Numerical investigation of the flow dynamics past a three-element aerofoil. *J. Fluid Mech.* **732**, 401–444 (2013). <https://doi.org/10.1017/jfm.2013.363>
- Deck, S., Renard, N.: Towards an enhanced protection of attached boundary layers in hybrid RANS/LES methods. *J. Comput. Phys.* (2019). <https://doi.org/10.1016/j.jcp.2019.108970>
- Deck, S., Renard, N., Laraufige, R., Sagaut, P.: Zonal Detached Eddy Simulation (ZDES) of a spatially developing flat plate turbulent boundary layer over the Reynolds number range  $3\ 150 < Re_0 < 14\ 000$ . *Phys. Fluids* **26**, 025116 (2014). <https://doi.org/10.1063/1.4866180>
- Deck, S., Gand, F., Brunet, V., Khelil, S.B.: High-fidelity simulations of unsteady civil aircraft aerodynamics: stakes and perspectives. Application of Zonal Detached Eddy Simulation. *Phil. Trans. r. Soc. A* **372**(2022), 20130325 (2014). <https://doi.org/10.1098/rsta.2013.0325>
- Deck, S., Weiss, P.-E., Renard, N.: A rapid and low noise switch from RANS to WMLES on curvilinear grids with compressible flow solvers. *J. Comput. Phys.* **363**, 231–255 (2018). <https://doi.org/10.1016/j.jcp.2018.02.028>
- Delrieux, Y., Prieur, J., Rahier, G., Drousie, G.: A new implementation of aeroacoustic integral method for supersonic deformable control surfaces. in 9th AIAA/CEAS Aeroacoustics Conference & Exhibit, AIAA Paper 2003–3201, (2003)
- Fadlun, E., Verzicco, R., Orlandi, P., Mohd-Yusof, J.: Combined immersed-boundary finite-difference methods for three-dimensional complex flow simulations. *J. Comput. Phys.* **161**, 35 (2000). <https://doi.org/10.1006/jcph.2000.6484>
- Faranosov, G., Belyaev, I., Kopiev, V., Bychkov, O.: Azimuthal structure of low-frequency noise of installed jet. *AIAA J.* **57**, 1885–1898 (2019)
- Ffowcs Williams, J.E., Hall, L.H.: Aerodynamic sound generation by turbulent flow in the vicinity of a scattering half plane. *J. Fluid Mech.* **40**(04), 657 (1970). <https://doi.org/10.1017/S0022112070000368>
- Ffowcs Williams, J.E., Hawkins, D.L.: Sound generation by turbulence and surfaces in arbitrary motion. *Phil. Trans. Royal Soc. London Ser. A Math. Phys. Sci.* **264**(1151), 321–342 (1969). <https://doi.org/10.1098/rsta.1969.0031>
- Fosso Pouangué, A., Sanjosé, M., Moreau, S., Daviller, G., Deniau, H.: Subsonic jet noise simulations using both structured and unstructured grids. *AIAA J.* **53**(1), 55–69 (2015). <https://doi.org/10.2514/1.J052380>
- Freund, J.B.: Noise sources in a low-Reynolds-number turbulent jet at Mach 0.9. *J. Fluid Mech.* **438**, 277–305 (2001)
- Gand, F.: Zonal Detached Eddy Simulation of a civil aircraft with a deflected spoiler. *AIAA J.* **51**, 697–706 (2013)
- Gand, F., Brunet, V.: “Zonal Detached Eddy Simulation of the flow downstream of a spoiler using the chimaera method,” in *Progress in Hybrid RANS-LES Modelling*. NNFM **117**, 389–399 (2012)
- Gand, F., Huet, M.: On the generation of turbulent inflow for hybrid RANS/LES jet flow simulations. *Comput. Fluids* **216**, 104816 (2021). <https://doi.org/10.1016/j.compfluid.2020.104816>
- Gand, F., Huet, M., Le Garrec T., Cléro, F.: Jet noise of a UHBR nozzle using ZDES: external boundary layer thickness and installation effects. in 23rd AIAA/CEAS Aeroacoustics Conference, AIAA Paper 2017–3526, (2017)
- Head, R., Fisher, M.: Jet surface interaction noise—analysis of far-field low frequency augmentations of jet noise due to the presence of a solid shield. in Proceedings of the 3rd Aeroacoustics Conference, AIAA Paper 1976–502, (1976)
- Housman, J.A., Stich, G.D., Kiris, C.K.: Jet noise prediction using hybrid RANS/LES with structured over-set grids. in 23rd AIAA/CEAS Aeroacoustics Conference, AIAA AVIATION Forum. AIAA Paper 2017–3213, (2017). <https://doi.org/10.2514/6.2017-3213>.

- Labbé, O., Peyret, C., Rahier, G., Huet, M.: A CFD/CAA coupling method applied to jet noise prediction. *Comput. Fluids* **86**, 1–13 (2013)
- Laraufie, R., Deck, S.: Assessment of Reynolds stresses tensor reconstruction methods for synthetic turbulent inflow conditions. Application to hybrid RANS/LES methods. *Int. J. Heat Fluid Flow* **42**, 68–78 (2013). <https://doi.org/10.1016/j.ijheatfluidflow.2013.04.007>
- Laraufie, R., Deck, S., Sagaut, P.: A dynamic forcing method for unsteady turbulent inflow conditions. *J. Comput. Phys.* **230**, 8647–8663 (2011). <https://doi.org/10.1016/j.jcp.2011.08.012>
- Lawrence, J.: Aeroacoustic interactions of installed subsonic round jets, University of Southampton, Institute of Sound and Vibration Research, PhD Thesis (2014)
- Lawrence, J.L.T., Azarpeyvand, M., Self, R.H.: Interaction between a Flat Plate and a Circular Subsonic Jet. in Proceedings of the 17th AIAA/CEAS Aeroacoustics Conference, Paper AIAA 2011–2745 (2011)
- Lighthill, M.J.: On sound generated aerodynamically II. Turbulence as a source of sound. *Proc. R. Soc. Lond. Ser. A* **222**, 1–32 (1954)
- Lorteau, M., Cléro, F., Vuillot, F.: Analysis of noise radiation mechanisms in hot subsonic jet from a validated Large Eddy Simulation solution. *Phys. Fluids* (2015). <https://doi.org/10.1063/1.4926792>
- Lorteau, M., de la Llave Plata, M., Couaillier, V.: Turbulent jet simulation using high-order DG methods for aeroacoustic analysis. *Int. J. Heat Fluid Flow* **70**, 380–390 (2018). <https://doi.org/10.1016/j.ijheatfluidflow.2018.01.012>
- Lorteau, M., Cléro, F., Vuillot, F.: Recent progress in LES computation for aeroacoustics of turbulent hot jet. Comparison to experiments and near field analysis. in 20th AIAA/CEAS Aeroacoustics Conference, Paper AIAA 2014–3057, (2014)
- Lyrntz, A.S.: Review: the use of Kirchhoff's method in computational aeroacoustics. *J. Fluid Eng.* **116**, 665–676 (1994)
- Lyu, B., Dowling, A.P.: Modelling installed jet noise due to the scattering of jet instability waves by swept wings. *J. Fluid Mech.* **870**, 760–783 (2019)
- Lyu, B., Dowling, A.P., Naqavi, I.: Prediction of installed jet noise. *J. Fluid Mech.* **811**, 234–268 (2017)
- Lyubimov, D., Maslov, V., Mironov, A., Secundov, A., Zakharov, D.: Experimental and numerical investigation of jet flap interaction effects. *Int. J. Aeroacoustics* **13**, 275–302 (2014)
- Mary, I., Sagaut, P.: Large Eddy Simulation of flow around an airfoil near stall. *AIAA J.* **40**, 1139–1145 (2002)
- Meloni, S., Mancinelli, M., Camussi, R., Huber, J.: Wall-pressure fluctuations induced by a compressible jet in installed configuration. *AIAA J.* **58**, 2991–3000 (2020)
- Mittal, R., Iaccarino, G.: Immersed boundary methods. *Ann. Rev. Fluid Mech.* (2005). <https://doi.org/10.1146/annurev.fluid.37.061903.175743>
- Mochel, L., Weiss, P.E., Deck, S.: Zonal immersed boundary conditions: application to a high-reynolds-number afterbody flow. *AIAA J.* **10**(2514/1), J052970 (2014)
- Nogueira, P.A.S., Cavalieri, A.V.G., Jordan, P.: A model problem for sound radiation by an installed jet. *J. Sound Vib.* **391**, 95–115 (2017)
- Perrino, M.: An experimental study into pylon, wing, and flap installation effects on jet noise generated by commercial aircraft, University of Cincinnati, PhD Thesis, (2014)
- Piantanida, S., Jaunet, V., Huber, J., Wolf, W.R., Jordan, P., Cavalieri, A.V.G.: Scattering of turbulent-jet wavepackets by a swept trailing edge. *J. Acoust. Soc. Am.* **140**, 4350–4359 (2016)
- Pont, G., Brenner, P., Cinnella, P., Maugars, B., Robinet, J.-C.: Multiple-correction hybrid k-exact schemes for high-order compressible RANS-LES simulations on fully unstructured grids. *J. Comput. Phys.* **350**, 45–83 (2017)
- Prieur, J., Rahier, G.: Aeroacoustic integral methods, formulation and efficient numerical implementation. *Aerosp. Sci. Technol.* **5**, 457–468 (2001)
- Rahier, G., Prieur, J., Vuillot, F., Lupoglazoff, N., Biancherin, A.: Investigation of integral surface formulations for acoustic post-processing of unsteady aerodynamic jet simulations. *Aerosp. Sci. Technol.* **8**, 453–467 (2004)
- Rahier, G., Huet, M., Prieur, J.: Additional terms for the use of Ffowcs Williams and Hawkings surface integrals in turbulent flows. *Comput. Fluids* **120**, 158–172 (2015)
- Rego, L., Avallone, F., Ragni, D., Casalino, D.: Jet-installation noise and near-field characteristics of jet–surface interaction. *J. Fluid Mech.* (2020). <https://doi.org/10.1017/jfm.2020.294>
- Renard, N., Deck, S.: Improvements in Zonal Detached Eddy Simulation for Wall Modeled Large Eddy Simulation. *AIAA J.* **53**(11), 3499–3504 (2015). <https://doi.org/10.2514/1.J054143>
- Sagaut, P., Deck, S., Terracol, M.: Multiscale and Multiresolution Approaches in Turbulence. Imperial College Press (2006). <https://doi.org/10.1142/p447>

- Shur, M.L., Spalart, P.R., Strelets, M.K.: Noise prediction for increasingly complex jets. part I: methods and tests. *Int. J. Aeroacoustics* **4**, 213–246 (2005a)
- Shur, M.L., Spalart, P.R., Strelets, M.K.: Noise prediction for increasingly complex jets. part II: applications. *Int. J. Aeroacoustics* **5**, 247–266 (2005b)
- Shur, M.L., Spalart, P.R., Strelets, M.K., Travin, A.K.: Synthetic turbulence generators for RANS-LES interfaces in zonal simulations of aerodynamic and aeroacoustic problems. *Flow Turbul. Combust.* **93**, 63–92 (2014)
- Spalart, P.R., Allmaras, S.R.: A one-equation turbulence model for aerodynamic flows. *La Recherche Aéronautique* **1**, 5–21 (1994)
- Spalart, P., Jou, W., Strelets M., Allmaras, S.: Comments on the feasibility of LES for wings, and on a hybrid RANS/LES approach, in *First AFOSR International Conference on DNS/LES.*, 1997.
- Stich, G.D., Housman, J.A., Kocheemoolayil, J.G., Kiris, C.C., Bridges, J.E., Brown, C.A.: Hybrid RANS/LES simulation of jet surface interaction noise. in 25th AIAA/CEAS Aeroacoustics Conference, AIAA Paper 2019b-2475 (2019b). <https://doi.org/10.2514/6.2019-2475>.
- Stich, G.D., Housman, J.A., Ghate, A.S., Kiris, C.C.: Jet noise prediction with Large-Eddy Simulation for chevron nozzle flows. in AIAA Scitech 2021 Forum. AIAA Paper 2021–1185 (2021) <https://doi.org/10.2514/6.2021-1185>
- Tam, C.K.W.: A phenomenological approach to jet noise: the two-source model. *Philosophical Transactions of the Royal Society A*. 377, (2019a)
- Tyacke, J.C., Wang, Z.-N., Tucker, P.G.: LES–RANS of installed ultra-high-bypass-ratio coaxial jet aeroacoustics with flight stream. *AIAA J.* **57**, 1215–1236 (2019)
- Uzun, A., Hussaini, M.Y.: Simulation of noise generation in near-nozzle region of a chevron nozzle jet. *AIAA J.* **47**, 1793–1810 (2009)
- Uzun, A., Hussaini, M.Y.: Prediction of noise generated by a round nozzle jet flow using computational aeroacoustics. *J. Comput. Acoust.* **19**, 291–316 (2011)
- van der Velden, W.C.P., Casalino, D., Gopalakrishnan, P., Jammalamadaka, A., Li, Y., Zhang, R., Chen, H.: Validation of jet noise simulations and resulting insights of acoustic near field. *AIAA J.* **57**, 5156–5167 (2019)
- Vera, J., Self, R.H., Kingan, M.J.: The prediction of the radiated pressure spectrum produced by jet-wing interaction. in Proceedings of the 21st AIAA/CEAS Aeroacoustics Conference, AIAA Paper 2015–2216, (2015)
- Wang, Z.-N., Proenca, A., Lawrence, J., Tucker, P.G., Self, R.: Large-Eddy-Simulation prediction of an installed jet flow and noise with experimental validation. *AIAA J.* **58**, 2494–2503 (2020)
- Zaman, K.B.M.Q.: Far-field noise of a subsonic jet under controlled excitation. *J. Fluid Mech.* **152**, 83–111 (1985)
- Zaman, K.B.M.Q.: Effect of initial condition on subsonic jet noise. *AIAA J.* **23**, 1370–1373 (1985)
- Zhu, M., Pérez Arroyo, C., Fosso Pouangué, A., Sanjosé, M., Moreau, S.: Isothermal and heated subsonic jet noise using Large Eddy Simulations on unstructured grids. *Comput. Fluids* **171**, 166–192 (2018)